Politecnico di Torino

Master's Degree in Aerospace Engineering

Master's Degree Thesis

Experimental Analysis of Shear-Flow Effects on the Aerodynamics and Performance of a Propeller

Supervisors
Prof. Gioacchino CAFIERO
Sara MONTAGNER

Candidate
Elia Pio MOTTOLA

2024/2025

Abstract

In the field of helicopter aerodynamics, the proper characterization of the operational environment is essential in order to predict the interaction between the aircraft and the surrounding aerodynamic flow. This requirement becomes even more critical for multirotor drones, whose reduced dimensions make them more sensitive to atmospheric turbulence and velocity gradients. At the same time, the use of drones is rapidly expanding in sectors such as agriculture, civil engineering, logistics, and transportation, making a thorough understanding of the aerodynamic phenomena affecting their safety and performance increasingly necessary. This work focuses on the experimental analysis of the interaction between a small-scale propeller and two incoming flow conditions: uniform flow and shear flow. The experimental campaign was carried out in the indoor flight arena at Politecnico di Torino. The facility is equipped with a wind wall which allows us to generate controlled unsteady inflows. Using Particle Image Velocimetry we analyze the wake of a drone propeller and we evaluate its performances using a 6-axis load cell. The results include a detailed description of the wake, relevant for multirotor drone applications, and an evaluation of propulsive performance under different operating conditions. Data analysis allows quantification of the influence of shear flow on propulsive behavior and discussion of the main aerodynamic effects involved, highlighting key aspects and future research directions.

Part I.
Introduction

In recent years, to cope with the growing request of increasingly confortable and fast services, a new transport mode emerged, which is Urban Air Mobility (UAM). This technology should be able to facilitate tasks such as small package delivery, urban transport, surveillance and even small vehicles for planetary exploration. This is precisely where the application of propellers comes in: these propellers can be ducted and unducted, and consequently undergo interaction with air flows or gusts.

Propulsive efficiency, dynamic response and performance under non-uniform flow conditions are key parameters for the design and optimisation of such systems. The study of the interactions between various types of propellers and incident flows, the characterisation of the wake generated and the determination of the forces acting on the propeller under various conditions assume an important role in this field and are precisely the subject of the study in this work.

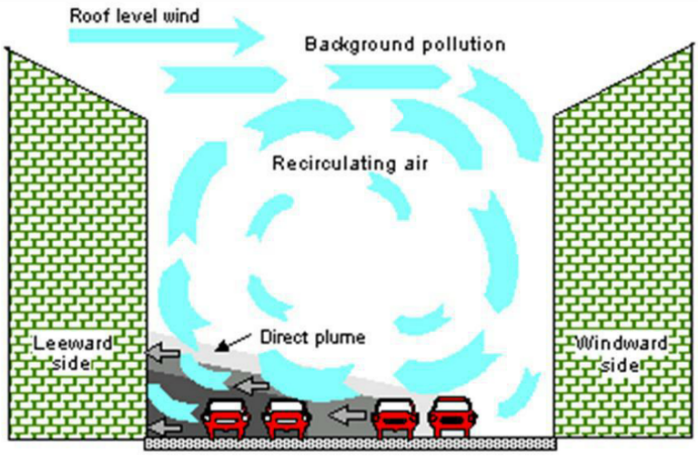

Figure 1: Example of urban environment affected by shear flow conditions [1].

The available literature on the subject is extensive and presents various case studies, including gust and shear flow cases, and some of them will be presented in the following. The focus of this work is to analyze the performance and the wake topology of a drone propeller in forward flight configuration when it's invested by a shear inflow. This condition is typical of numerous environments, urban and extra-urban, where drones find application: these scenarios include flight close to the ground, environments with strong atmospheric wind gradients, and also interaction with other rotors or load-bearing surfaces. This leads to a variation in propeller behaviour, affecting load distribution along the blades and thus performance. Figure 1 shows a typical urban environment, known as an 'urban canyon'. This condition occurs when a narrow street is flanked by tall buildings, creating air recirculation that can cause shear flow. Figure 2 shows instead the pattern of a phenomenon typical of extra-urban environments, called "Sea Breeze Shear": this phenomenon is generated by the interaction between the sea breeze, which moves from the ocean towards the land during daylight hours, and the atmospheric winds present at higher altitudes. This interaction creates a marked gradient in wind speed and direction, with intense vertical

shear values.

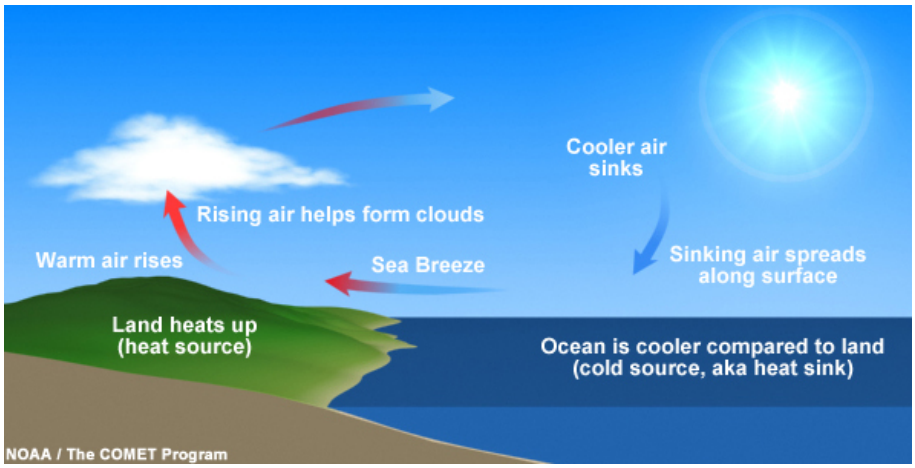

Figure 2: Example or natural environment affected by shear flow condition, sea breeze shear [2].

These topics will be addressed in this paper and analysed through a primarily experimental approach, using the instrumentation available in the Modesto Panetti gasdynamics laboratory at the Politecnico di Torino. The main objective is to study the behaviour of two propellers of different sizes subjected to uniform wind and to shear flow generated by a dedicated facility, in order to detect possible differences in their behaviour and performance. Understanding whether such differences exist and whether they have a significant impact on the operation of the component is important to limit risks and improve the technology.

The work is structured as follows:

- Part II deals with the introduction of the theoretical background and the state of the art, analysing the existing literature, referring to the main theories and experimental results already available;
- Part III contains an accurate description of the instrumentation used, as well as the various measurement setups;
- Part IV presents and discusses the experimental results obtained;
- Part V summarises the main conclusions of the work.

Introduction to propeller physics

The element of greatest interest within the propeller system is obviously the propeller, which produces the thrust T and the resistant torque Q. There are numerous types of propellers with different purposes and therefore different geometries: the propeller's performance is defined precisely by the aerodynamic forces produced by the rotation and therefore by the coefficients that normalise them.

We can therefore briefly summarise the normalised parameters that define the behaviour of these components and will be of interest for the present work.

- Advance Ratio J

$$J = \frac{V_\infty}{ND}$$

Where V_∞ is the speed of the undisturbed flow, N is the propeller rotation speed (rev/s) and D is the propeller diameter.

This parameter can be interpreted as the normalised pitch of the propeller, i.e. a dimensionless parameter that compares translational and rotational motion. J is also related to the rotational speed of the propeller $\Omega = 2\pi N$

$$J = \pi \frac{V_\infty}{\Omega R}$$

Where R is the propeller radius.

- Thrust coefficient C_t and Torque coefficient C_q:

$$C_t = \frac{T}{\rho N^2 D^4}$$

$$C_q = \frac{Q}{\rho N^2 D^5}$$

- Power coefficient C_P

$$C_P = \frac{P}{\rho N^3 D^5} = \frac{Q\Omega}{\rho N^3 D^5} \Longrightarrow 2\pi C_q$$

- Propulsive efficiency η, ratio of available power to shaft power:

$$\eta = \frac{P_a}{P} = \frac{TV_\infty}{Q\Omega} \Longrightarrow \frac{J}{2\pi}\frac{C_t}{C_q}$$

Although these performance parameters are characterised by six parameters, it is possible to reduce this dependence to three variables by means of dimensional analysis. One of these variables is J, while the other two are the Mach number M and Reynolds number Re. These parameters will be defined later as a reference for the description of the experimental data.

Part II.
Relevant Literature

Technological context

Various papers concerning this topic are referred to drones: this type of vehicle is gaining more and more importance in multiple fields, like urban air mobility and military applications. This is the starting point to understand why it is important to study the response of various type of propellers, exposed to different external conditions. Susini [3] reports that 400 large US military drones have crashed in major accidents since 2001, while the risk is rising over the past decade as the military has expanded drone mission frequency. The accidents occur both in military and civil operating zones and can be grouped into two main categories:

- Class A accidents, with complete destruction of the UAV and 2 million US dollars damage (192 crashes);
- Class B accidents, with complete or partial destruction of the UAV and between 2 and 5 million US dollars damage (224 crashes).

One of the safety gaps that need to be overcome by the manufacturers is located during landing phase: this is just an example of how important it can be to analyze and predict forces and torques on the drones's propellers in various wind conditions, also to help in development of adequate control systems.

Effect of freestream on propeller performance: analytical model

A first step in analysing propeller performance can be taken through the paper of Hedayatpour et al. [4]. The author describes how, in literature, propeller thrust and torque are typically modelled as proportional to the square of angular velocity, and freestream effects are neglected by assuming low velocities, thus noting the need to develop a suitable model for propeller analysis. Freestream can in fact influence propeller performance in two main ways:

- Changing the angle of attack of the blades;
- Changing the local speed on the blade profile.

The presence of these two effects is analysed in Hedayatpour's work, which uses an analytical approach, through Blade Element Theory (BET), to calculate performance on a generic propeller.. In fact, it describes the effects of freestream on propeller performance, both for the cases of velocity vector perpendicular and parallel to angular velocity vector of the propeller.

For the first case we refer to Figure 3: a propeller rotates at angular velocity ω_p, with two blades of radius R_b and assuming a constant chord c. For simplicity, the freestream is considered uniform with velocity vector $V_{\infty 1}$ parallel to the y-axis. Considering a blade element, it will have length c and differential width dr_b, with r_b being the distance of the blade element from the centre of the propeller. Due to the rotation of the propeller, a

relative air flow velocity with modulus $r_b \|\omega_p\|$ is generated on each blade element. For the advancing blade ($0 \leq \psi_p \leq \pi$) the freestream velocity increases the relative air flow velocity over the blade, while for the retreating blade ($\pi \leq \omega_p \leq 2\pi$) decreases the relative air flow velocity.

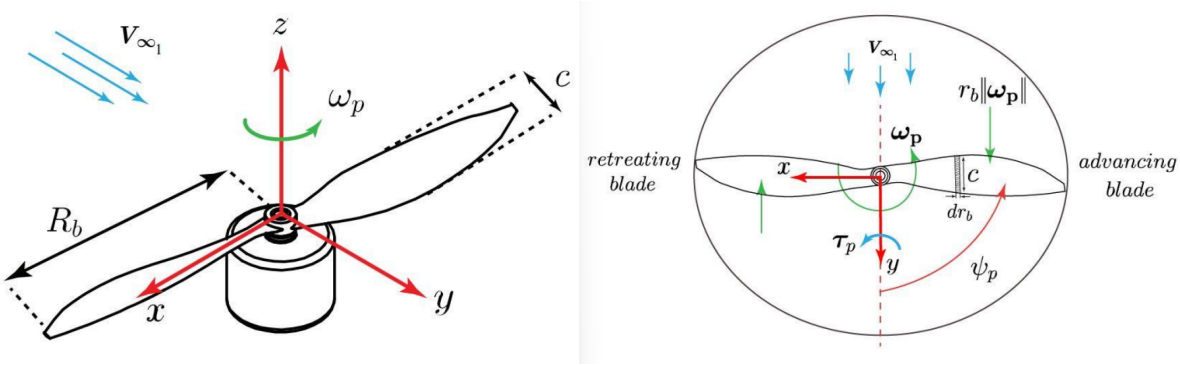

Figure 3: Propeller in presence of perpendicular freestream [4].

Therefore, defining the azimuth angle ψ_p as the angle between the freestream direction and the blade, the resulting velocity will be

$$v = r_b\|\omega_p\| + \|V_{\infty 1}\| sin\psi_p$$

This effect cause the generation of a moment τ_p in direction of the freestream velocity, due to change in thrust force with respect to ψ_p.

Once the speed has been defined, the thrust and torques along z and y for each blade element are calculated using BET:

$$df_p = \frac{1}{2}\rho_a c C_L v^2 dr_b$$

$$d\tau_{d_p} = \frac{1}{2}\rho_a c C_D v^2 r_b dr_b$$

$$d\tau_p = \frac{1}{2}\rho_a c C_L v^2 sin\psi_p dr_b$$

By integrating along the radius r_b and azimuth angle ψ_p, it is possible to obtain the average quantities: results show (Figure 4) that in presence of a freestream velocity $V_\infty \neq 0$, the average thrust force of the propeller, the average moment τ_{d_p} (moment due to drag force of the blade element) and the average τ_p all increase, while the actual quantities have a sinusoidal trend with ψ_p.

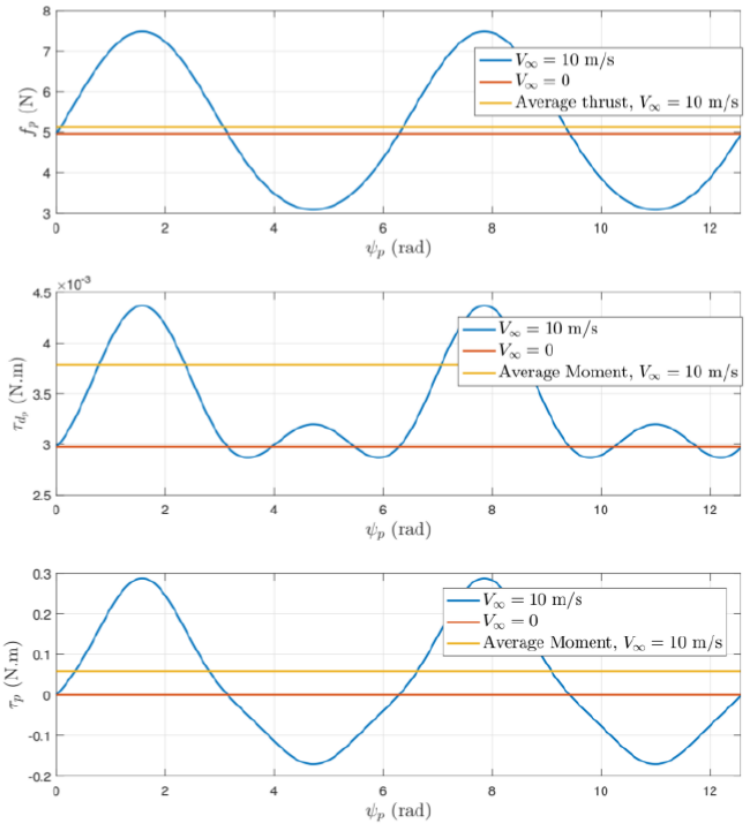

Figure 4: Thrust force and moments of a propeller in presence of freestream [4].

The study proceeds with the analysis of the case with freestream velocity vector in parallel with angular velocity vector of the propeller. Consider a propeller rotating at angular velocity ω_p: on each blade element, the airflow velocity vector $r_b\omega_p$ is indicated in green and the angle of attack Θ is defined as the angle between the chord of the blade element and the local airflow velocity vector $r_b\omega_b$.

As shown in Figure 5, the freestream changes the magnitude and direction of the resultant airflow velocity: the new blade angle of attack Θ' will be greater or smaller than Θ for the cases of positive freestream or negative windstream respectively. The angle of attack Θ directly affects the C_L of the blade element and so the thrust force generated by the propeller.

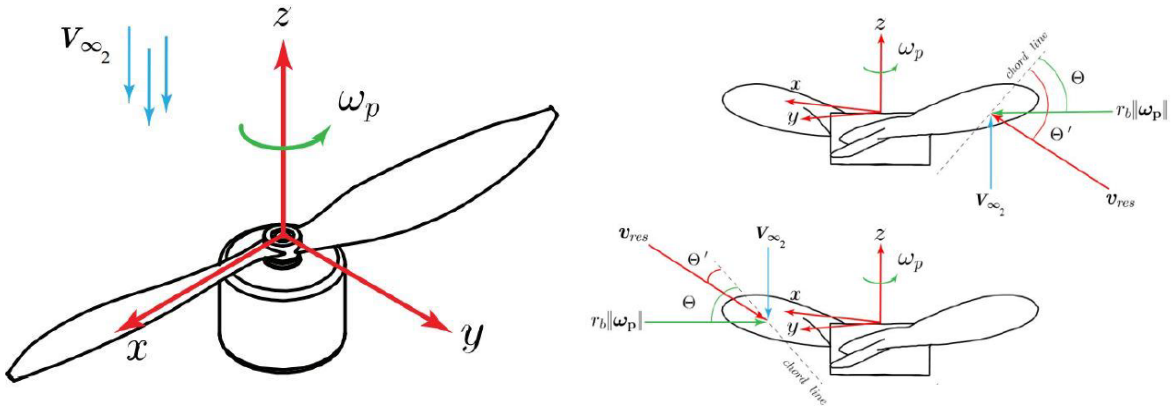

Figure 5: Propeller in presence of parallel freestream [4].

In particular for subsonic speed this relationship can be considered linear

$$\frac{\Delta C_L}{\Delta \Theta} = \sigma$$

where σ is an empirical constant. So a positive z component freestream velocity increases Θ that which increases thrust force, vice versa for a negative z component freestream velocity. The thrust force variation can be written as:

$$\Delta f_p = \frac{1}{4}\rho_a c \sigma R_b^2 \|V_{\infty 2}\| \|\omega_p\|$$

Effect of freestream on propeller performance: CFD model

In the case just analysed, we saw a generic propeller, analysed using blade element theory: we can therefore consider a case where a small commercial propeller is studied through a CFD analysis. Zhang et al. [5] describes an aerodynamic analysis of a small propeller, about 10 inches, in various wind conditions. The propeller for CFD simulation was generated with CATIA, with a CLARK-Y profile, and is set in motion using sliding mesh technology. This propeller system is contained within a cylindrical domain, which in turn is contained within a large "cuboid" domain where the effects of horizontal and vertical wind are applied. At this point, the mesh is obtained on the domain and the CFD is performed, using Detached-Eddy Simulation as a turbulence model, with 20 simulation steps equivalent to one second of propeller movement.

Among the results of this study, those relating to thrust are particularly significant: Figure 6 shows the thrust trend in relation to the propeller rotation speed for various vertical wind conditions, directed in the opposite direction to the thrust. The thrust value decreases as the wind intensity increases, by about 10 for a Δv of $2m/s$. There is an exception for high rotation speeds, where there is a significant reduction in thrust when moving from $v = 0$ to $v = 2m/s$. These high rotation speeds must therefore be avoided when flying outdoors.

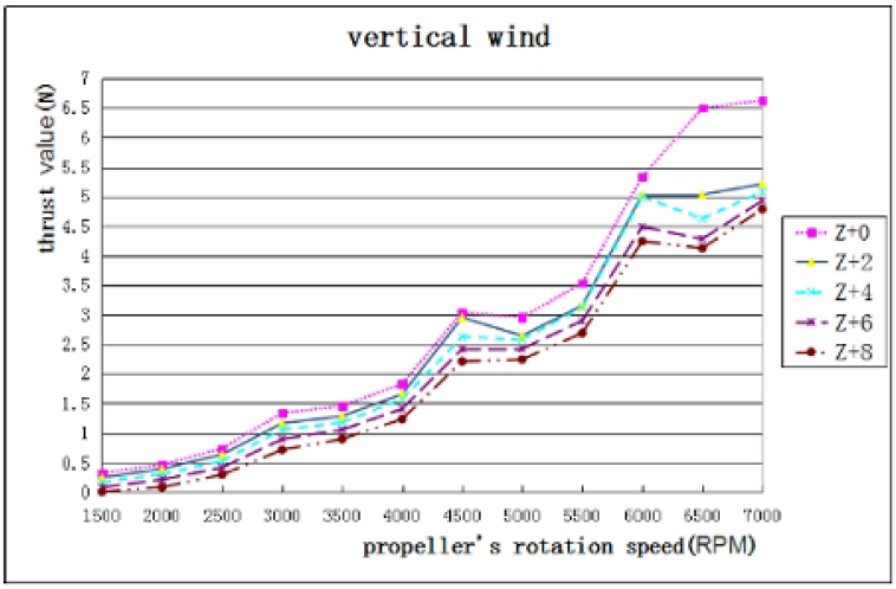

Figure 6: Thrust trend with rotational speed, vertical wind [5].

As regards the thrust trend with horizontal wind, this is shown in Figure 7. Although the effect is essentially the same as the one already reported for vertical wind, it can be seen that below $6000rpm$ the reduction in thrust is small and negligible. As regards high ω, the same reduction in thrust as in the case of vertical wind can be seen.

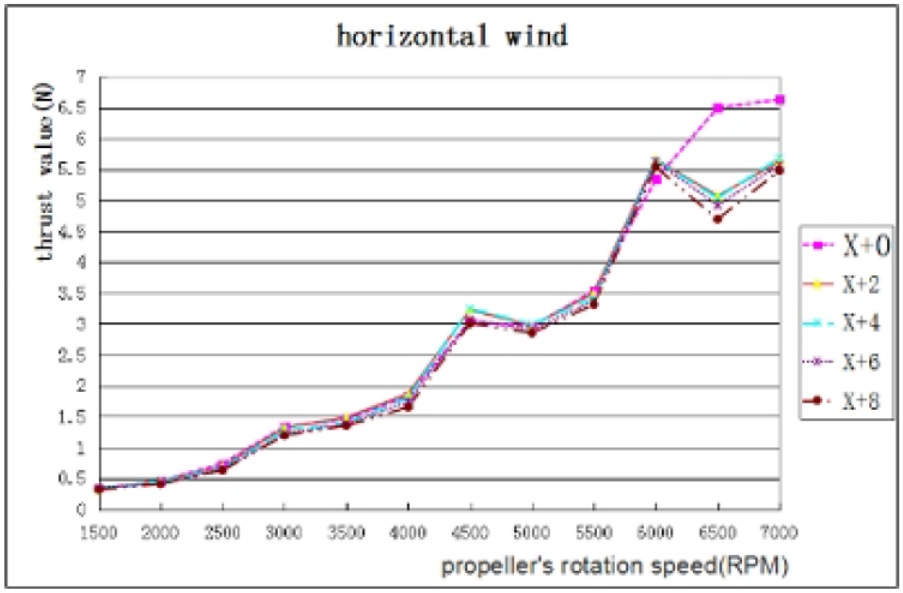

Figure 7: Thrust trend with rotational speed, horizontal wind [5].

Of particular interest is also the characterisation of aerodynamic forces over time in the case of horizontal wind, where the sinusoidal trends already seen in Hedayatpour's work reappear. In particular, Figure 8 shows the thrust at constant speed ($5500rpm$) as a function of time. As the wind intensity increases, both the amplitude and the maximum value of the sinusoid increase.

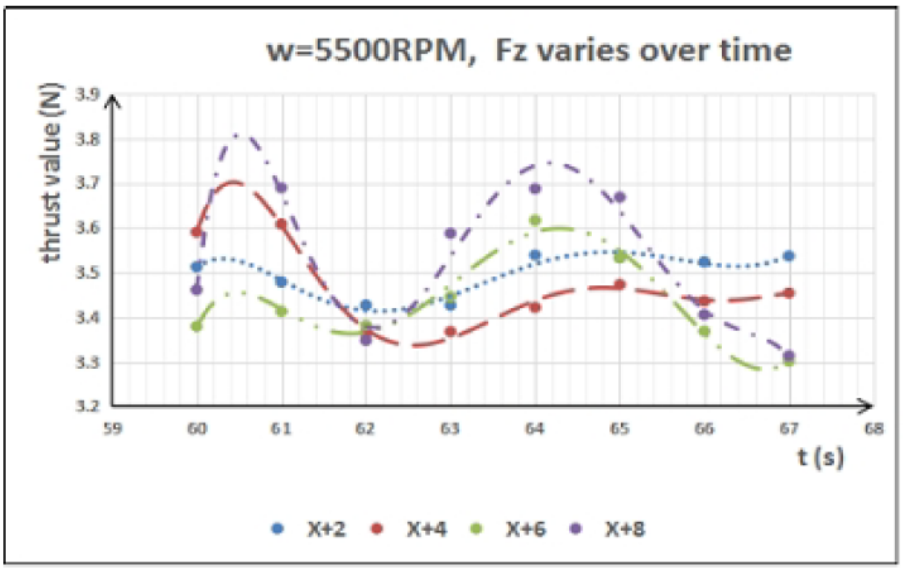

Figure 8: Thrust sinusoidal trend in time, horizontal wind, 5500rpm [5].

According to Zhang, in addition to thrust, it is important to evaluate the aerodynamic force F_x, i.e. the force parallel to the horizontal wind. Imagine a multirotor aircraft in hover mode: it is important to evaluate this aerodynamic effect in order to maintain the hovering position.

So, regarding F_x, it is possible to identify three classes of behavior:

- First class: from 1500rpm to 3000rpm, the F_x is generally negative (with the x axis parallel to the applied horizontal wind field).

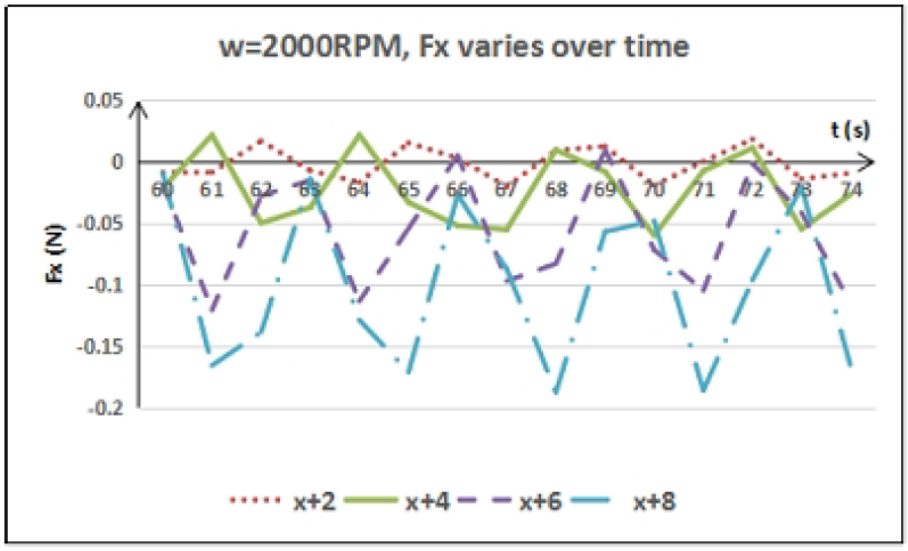

Figure 9: F_x - First class of behaviour [5].

- Second class: from 3500rpm to 4500rpm, F_x has negative peaks greater in absolute value of positive peaks.

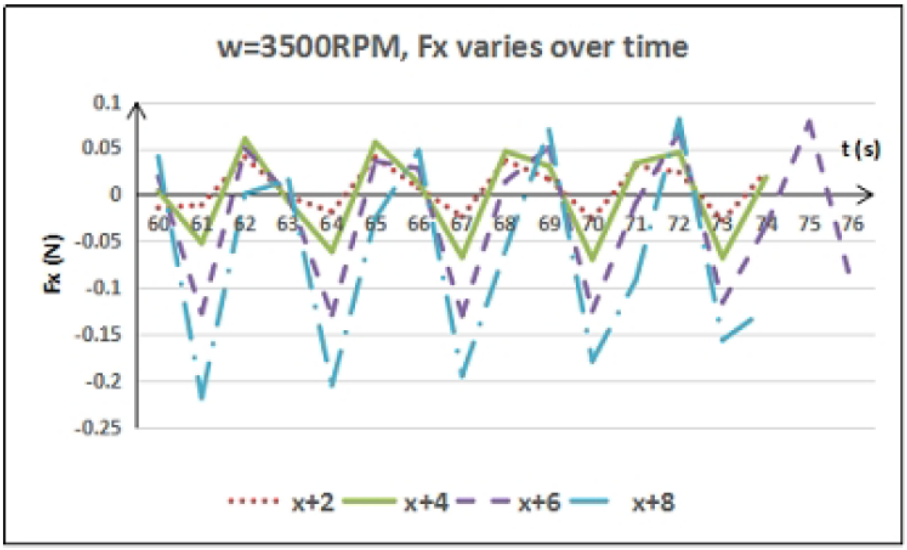

Figure 10: F_x - Second class of behaviour [5].

- Third class: from $5000rpm$ to $7000rpm$, F_x has negative peaks equal to positive peaks.

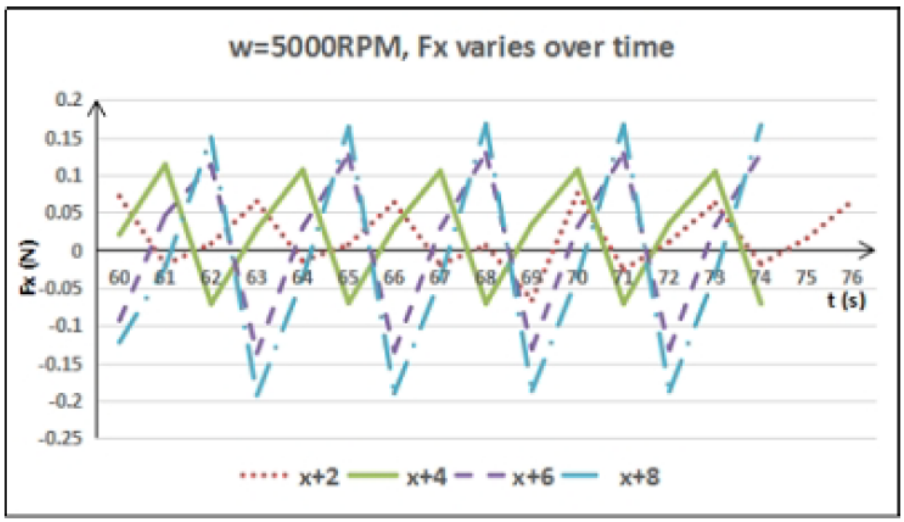

Figure 11: F_x - Third class of behaviour [5].

It is possible to fit the relation between F_x and horizontal wind velocity, for a fixed rotation speed, in a straight line (Figure 12). For first and second class, the slope increases with the increase of propeller's rotation speed, while for the third class we can see maximum slope for $5000rpm$.

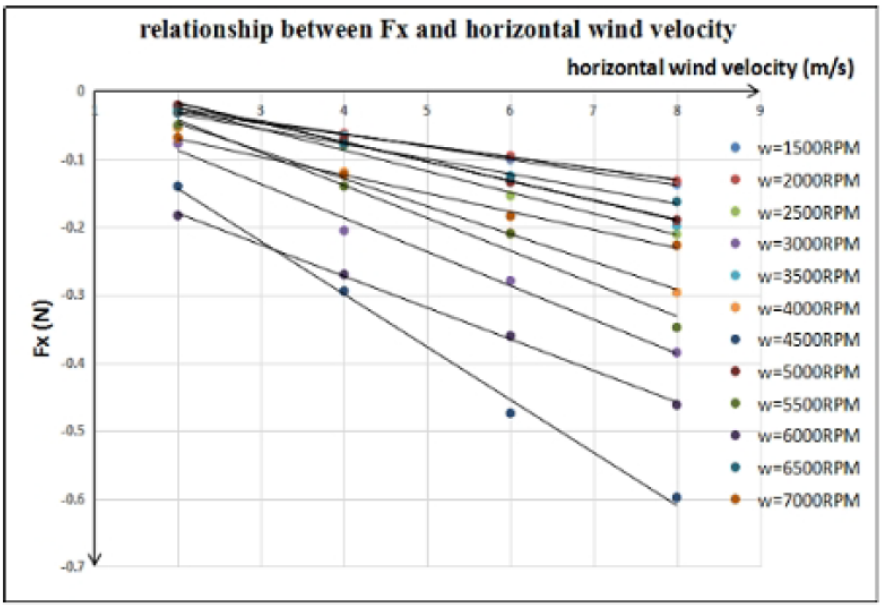

Figure 12: Relationship between F_x and horizontal wind velocity [5].

Effect of freestream and gust on propeller: comparison of numerical simulation and experimental data

Proceeding with the analisys of freestream-propeller interactions, Murakami et al. [6] investigated the effects of cross flow and fluctuating cross flow of multirotor drone propellers, using wind testing and numerical simulations.

Numerical simulations are used to validate experimental data and are carried out by combining Momentum Theory with Blade Element Theory: each section of the blade is modelled using equations derived from the aerodynamic coefficients of the profile. The local flow on the blade W is calculated, i.e. the relative velocity perceived by the blade at radial position r and azimuth angle (ψ) as

$$W(\psi) \cdot cos[\phi(\psi)] = r\Omega(1 - a'(\psi)) + usin\psi$$

- $[\phi(\psi)]$ is the local flow angle;
- Ω is the angular velocity of the rotor;
- a' is the interference factor in the tangential direction;
- u is the crossflow velocity.

The angle of attack, Reynolds number and force per unit radius are then evaluated locally and integrated to obtain thrust T and torque Q.

The experimental data is collected in a wind tunnel located at the National Institute of Advanced Industrial Science and Technology in Japan. The wind tunnel is an open-circuit type, with a section measuring $1.4m$ x $1.4m$: three different propellers with increasing diameters and different chord distribution were tested, connected to a support fixed to a 6-axis load cell.

So, during the experimental testing, thrust coefficient C_T and power coefficient C_P were measured and Figure of Merit FM (parameter related to propeller efficiency) were calculated, in various flow conditions. Then, results were verified through numerical simulations. Thrust and torque were measured, with an error within $\pm 0.5\%$, while the coefficient were evaluated by the equations

$$C_T = \frac{T}{\rho n^2 D^4}$$

$$C_P = \frac{\Omega Q}{\rho n^3 D^5}$$

$$FM = \frac{T\sqrt{\frac{T}{2\rho\pi R^2}}}{\Omega Q}$$

The flow conditions studied in the paper are two:

- Cross flow: stationary air current, striking the propeller laterally at a constant speed (various measurements, varying the speed from 0 to $10 m/s$) and constant direction.
- Fluctuating cross flow, i.e. a controlled gusty wind, which generates oscillations with a frequency of $0.5 Hz$ and variable intensity between 0 and $10 m/s$.

A first result concerns the FM, stating that this parameter increases with the increase of rotational speed and reaches the peak around the design condition. Furthermore, FM increases as the diameter increases.

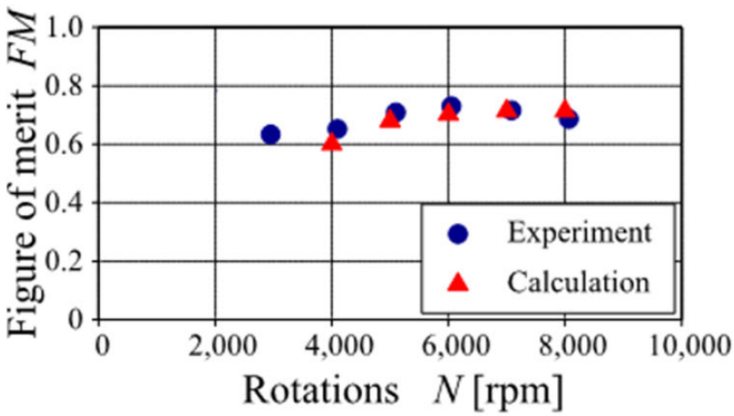

Figure 13: Relationship between rotational speed and FM [6].

Other important results are separated in the two cases of cross flow and fluctuating cross flow. The reference geometry is shown in Figure 14. Three points on the blade are considered, at $r = 0.2R$, $r = 0.6R$ and $r = 0.975R$: we will refer to them respectively as A, B and C.

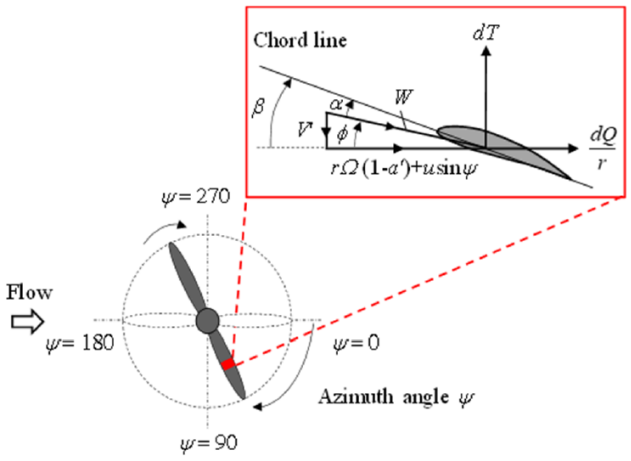

Figure 14: Axes and reference quantities for the study of the propeller under cross flow [6].

Thrust, angle of attack and Reynolds number under cross flow velocity increase compared to the case with $u = 0m/s$, during the advancing phase ($\psi = 0°$ to $\psi = 180°$) in B and C. Infact, the cross flow increases the relative flow velocity on the propeller during the advancing phase, while decreases the relative flow velocity during the retrating phase. However, the increase of thrust during the advancing phase is larger that the decrease in the retreating phase.

Similarly, for point A, thrust increases under cross flow compared to the case with $u = 0m/s$ in advancing phase, but with a small increase from $\psi = 25°$ to $\psi = 165°$. This phenomenon is related to the stall of the propeller during the advancing phase, which means that root of the propeller is more susceptible to cross flow, so the real change of the relative angle of attack at the root will be grater of the design value.

Local Reynolds number increase from A to B and decrease from B to C. The propeller does not genereate thrust during most of the retreating phase, due to the low Re of the propeller in this condition.

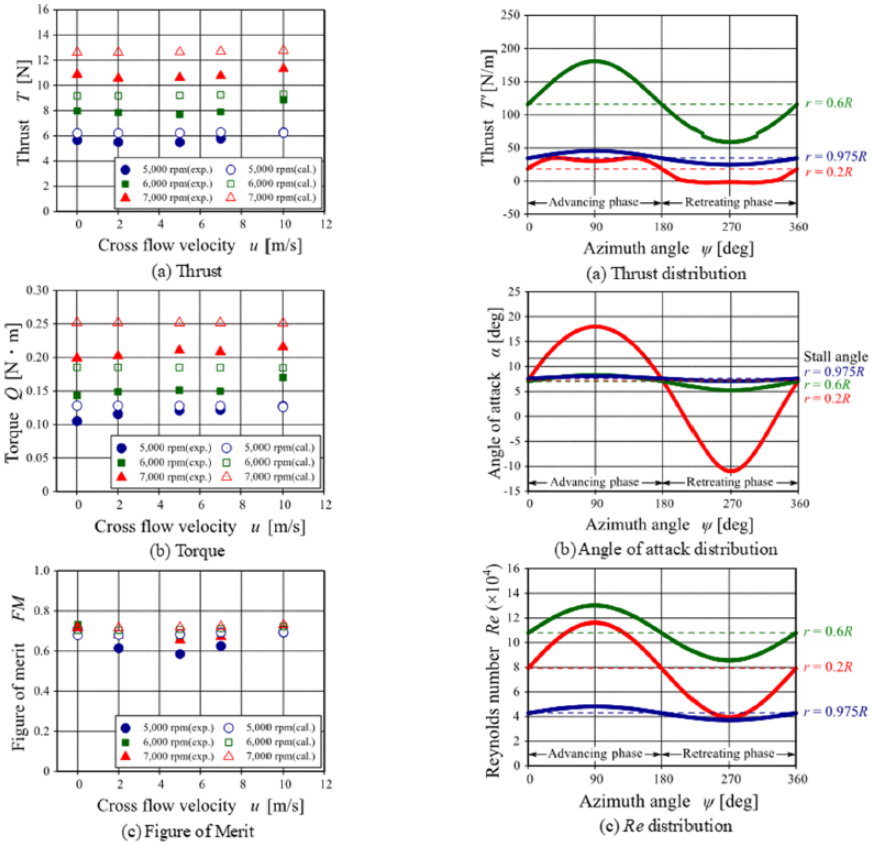

Figure 15: Various experimental results for cross flow [6].

Another important result can be found into the relationship between cross flow velocity and C_T. The propellers are more susceptible to cross flow at lower rotational speed, as C_T at $u = 10m/s$ at low rotational speed is much larger than at high rotational speed. The cross flow velocity becomes dominant compared to the peripheral velocity of the propeller while decreasing the rotational speed.

Speaking about the case of fluctuating cross flow, results state that magnitude of fluctuation in time-histories of C_T becomes large with increasing of speed. Furthermore, fluctuation of C_T reduces with increasiing of the rotational speed.

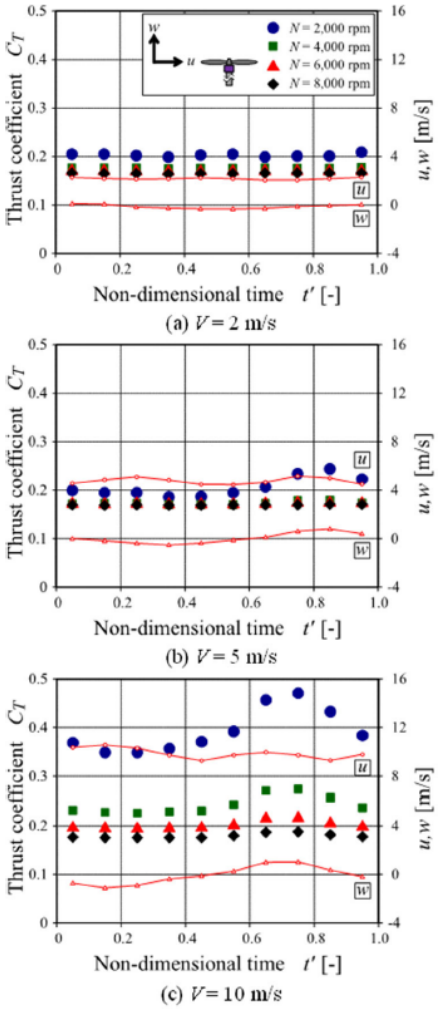

Figure 16: Relationship between fluctuating flow velocity and thrust coefficient [6].

Effect of gust on a helycopter rotor

Wang et al. [7] analyse the aeroelastic response of a helicopter rotor subjected to different vertical gust profiles, both in hovering and in forward flight. To do this, the authors develop a coupled aero-structural model that combines a medium deformation beam theory with a non-stationary aerodynamic model in the time domain. The gust is idealised as a uniform vertical velocity field over the entire disc, an assumption that allows the effect of unsteady aerodynamic forcing on the rotor response to be isolated. Through time integration using the Newmark scheme, the model consistently provides aerodynamic forces, elastic deflections and hub loads, allowing the transient evolution of thrust and shear stress to be derived. The data discussed by Wang are derived entirely from this coupled numerical model.

Wang report that dynamic load due to gust for helicopters affects rotors causing loss of trust force or the increase of deflection, leading to control instability or blade failure. Hence, this case of study is considered one of the most critical load cases in the design and certification of helycopter rotors. Moreover, Wang states that hover configuration for the rotor is interesting cause it is a limiting design point in terms of power requirements.

Moreover, the rotor operates usually in dynamic stall flow, while it's hard to describe the flux through the rotor, especially at the blade root and tip.

In the analysis Wang defines a gust model with three types of gust configuration, typical for helycopter rotors, assuming that the gust field is invariant in the space.

- Impulse-Shape gust, with a strength W and a duration time t;
- Slope-Shape gust, with a maximum strength W and slope lenght is t;
- 1-cos-Shape gust, with a strength W.

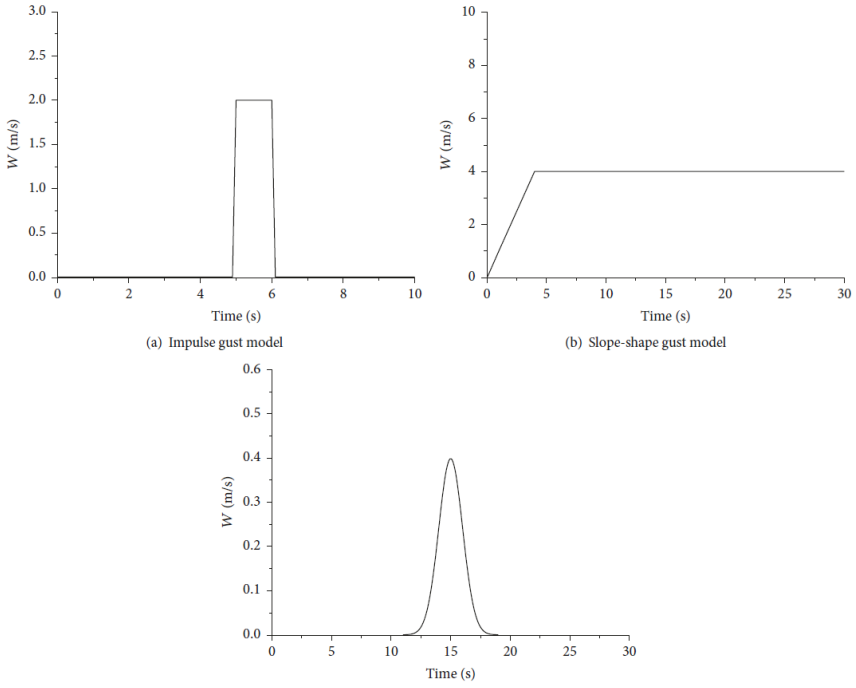

Figure 17: Gust models considered in the study [7].

Dyamic gust load for this cases is investigated, for an isolated rotor rotating at a speed of $383rpm$ and a downward gust, with an amplitude of $8m/s$. Gust response for hover ad forward flights has been calculated, for $J = 0.2$ and $J = 0.35$ respectively.

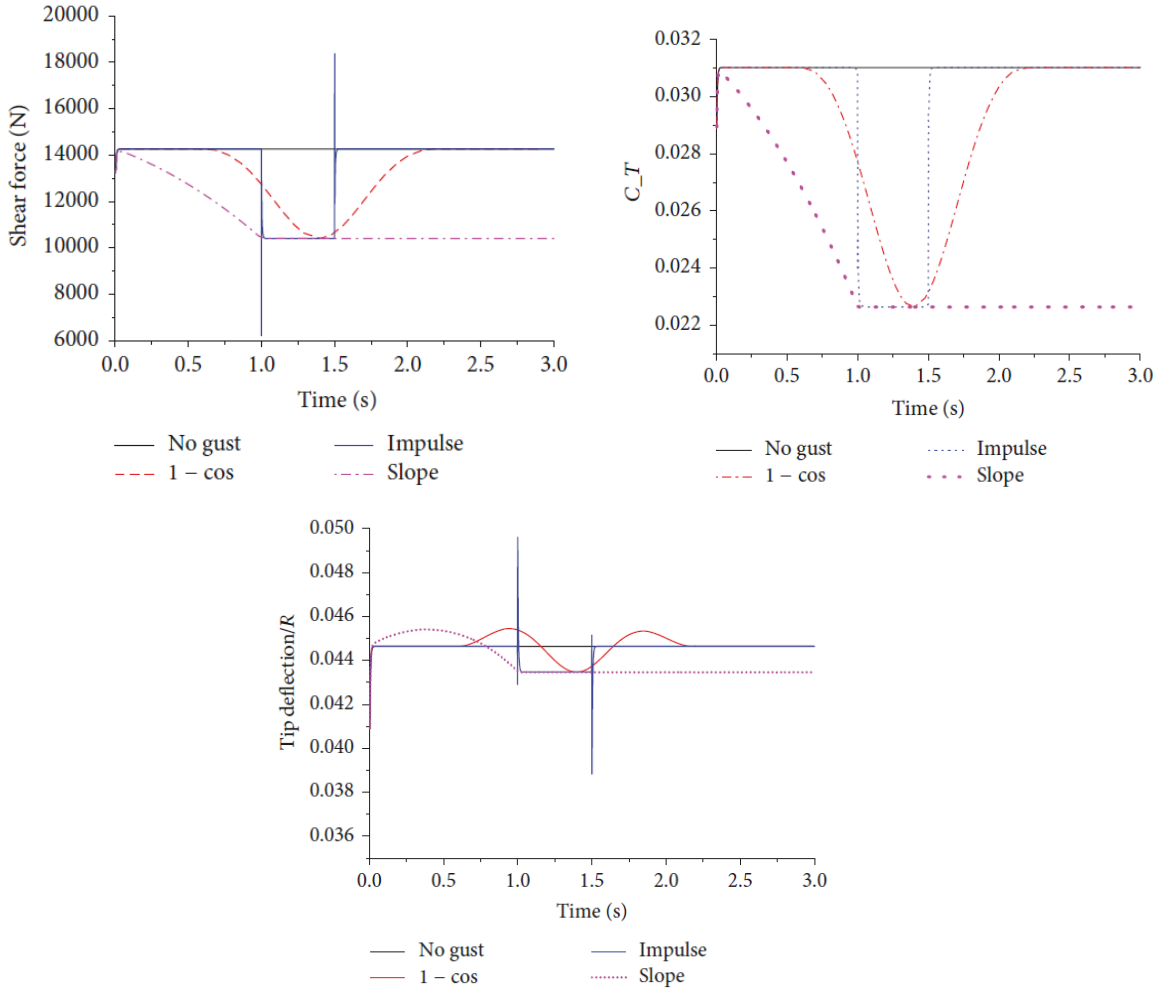

Figure 18: Shear force at the root of rotor, thrust coefficient on the rotor disk, tip deflection of rotor [7].

Results for the hover case are shown in Figure 18. Shear force keeps a fixed value in condition of no gust, decreasing as the gust velocity reaches the maximum. At the beginning and end of the impulse gust, the shear force presents a peak, due to instantaneous shock effect. Also, the C_T decrease with the intensity of the gust: at the maximum amplitude of the gust, the C_T is reduced to a quarter of the main value with no gust. Moreover, we can see the behaviour of the tip deflection: first it grows to a value higher than the main value, then it decreases below the main value with a minimum peak where the gust has a maximum peak and finally it rises above the main value to then stabilize at the end of the gust. Maximum peak is greater in the case of impulse gust.

Acting a multiscale 1-cos-Shape gust on the rotors allows to investigate the effect of the gust frequency.

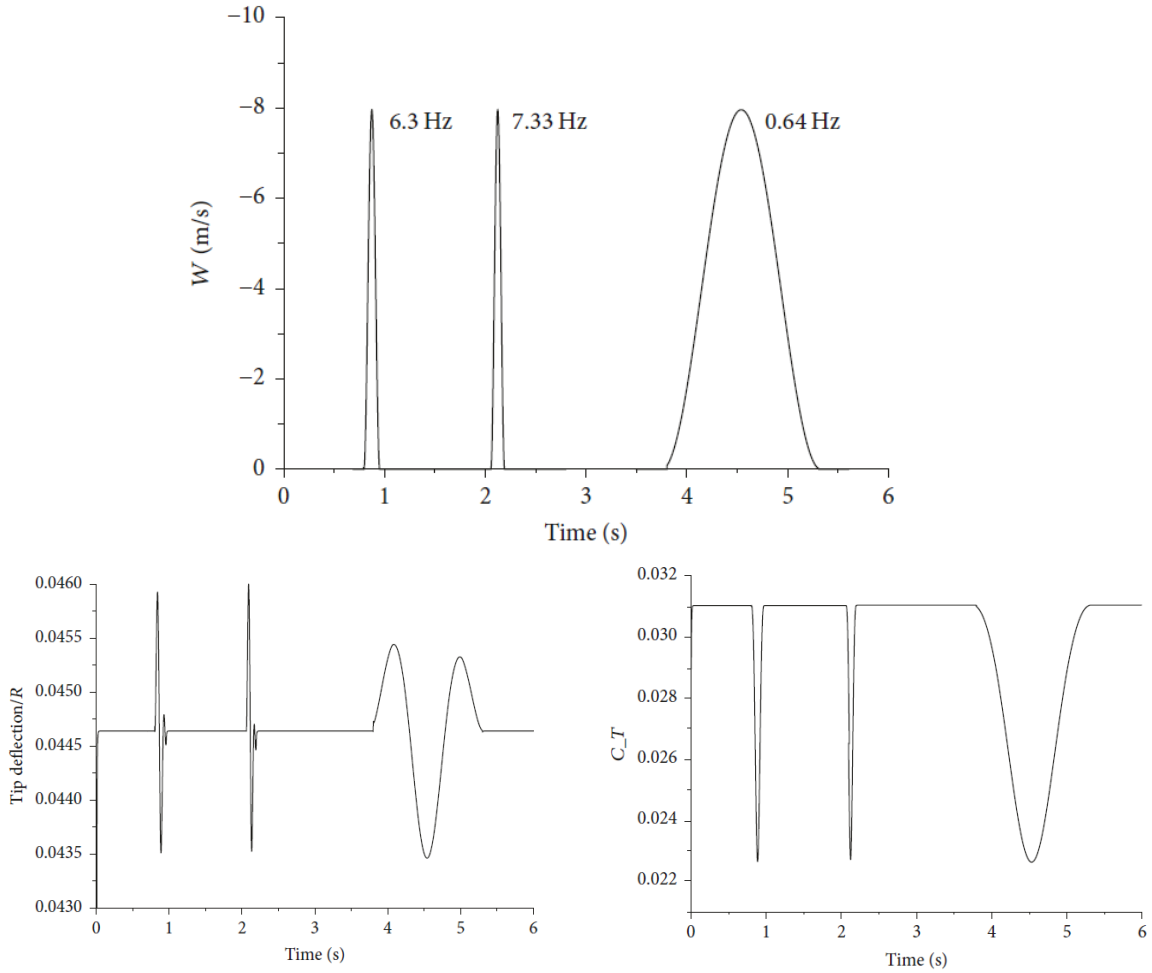

Figure 19: Multifrequency sinusoidal gust, with the tip deflection and the thrust coefficient trend [7].

As shown in Figure 19, minimum peaks of C_T remain the same as the gust frequency changes, while tip deflection maximum is increasing as the gust frequency increases.

Effect of shear flow on propeller

Kotb and Schetz [8] analyzed the three-dimensional velocity field in the wake of a three-bladed propeller with a diameter of $0.49m$. In particular, they measured the propeller thrust and torque under both uniform inflow and shear-flow conditions, and characterized the mean flow field using a five-hole probe. They also conducted turbulence measurements, evaluating turbulence intensity and the components of the Reynolds stress tensor, as well as characterizing the single-blade wake in terms of both mean-flow features and turbulent quantities.

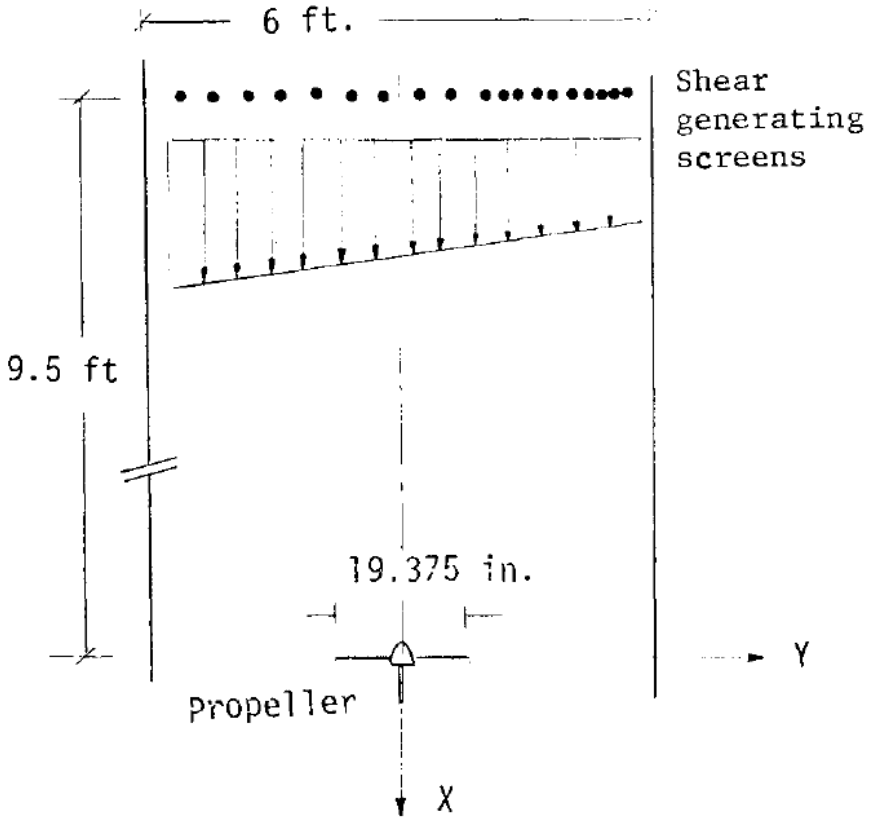

Figure 20: Wind tunnel test configuration for evaluating shear flow on propeller [8].

The experiments were conducted in Virginia Tech's $2x2$ wind tunnel, with a flow velocity of approximately $8.52m/s$ and very low background turbulence. The assembly of five grids with different mesh allows the generation of flow with a linear velocity gradient, with a slope of 0.0794. The propeller has a pitch of $P/D = 1.52$: the complete setup is shown in Figure 20.

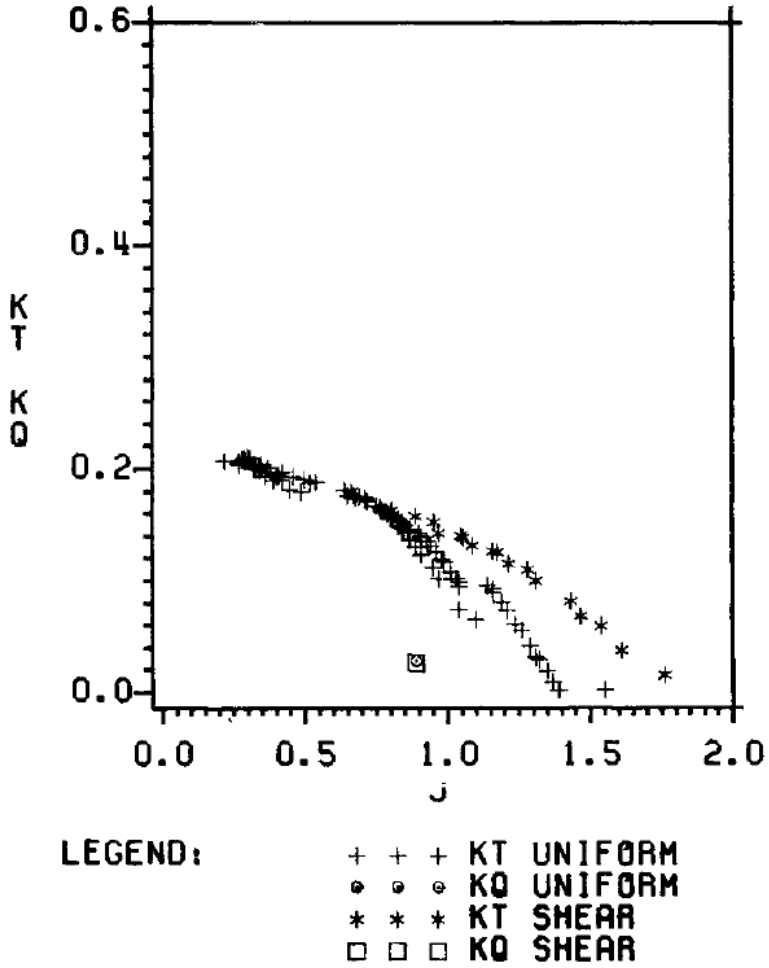

Figure 21: Thrust and torque coefficients, KT and KQ [8].

A first set of results shows the trends of the thrust and torque coefficients, KT and KQ. These are reported in Figure 21 as a function of the advance ratio J, computed using the centerline velocity (i.e., the freestream velocity in the uniform-flow case). For values of $J \leq 0.9$, the KT values remain similar between the uniform and shear-flow cases; once this threshold is exceeded, however, the curves diverge and the KT corresponding to the shear flow becomes higher than in the uniform case. At the operating point, a 17% increase in thrust is observed. According to the authors, this is due to the higher inflow velocity over part of the propeller disk in the presence of shear, which results in an effectively higher pitch ratio and therefore a slightly greater thrust.

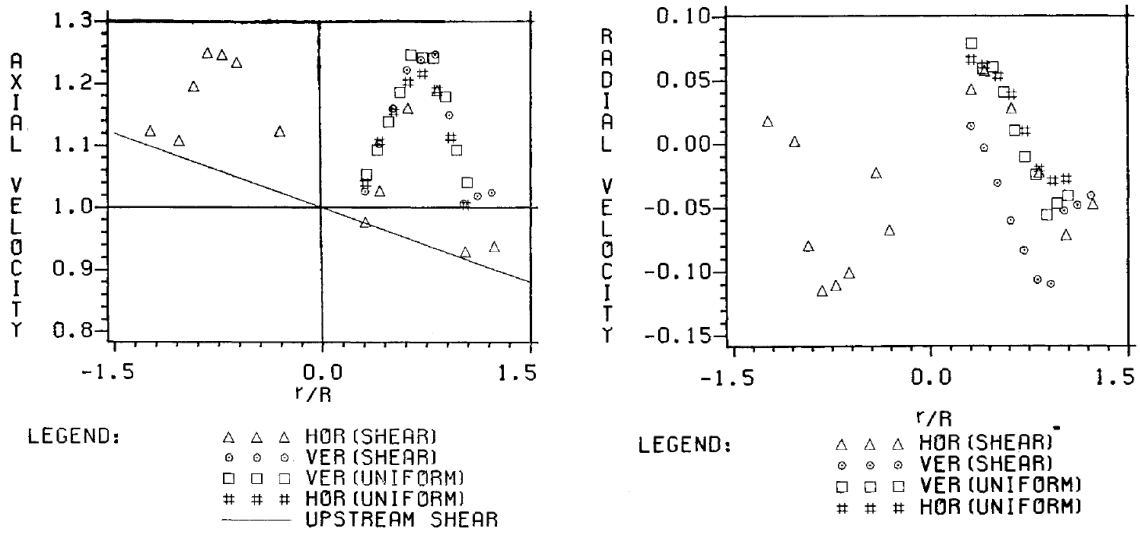

Figure 22: Axial (left) and radial (right) mean velocities [8].

Regarding the axial mean velocity measured downstream of the propeller ($X = 0.025D$), the results are shown in Figure 22 (left). The normalized velocity U/U_∞, referenced to the upstream freestream velocity, is plotted as a function of the radial position r/R, normalized by the propeller radius. The propeller increases the flow velocity downstream, and the shear-flow condition results in higher induced velocities than the uniform-flow case, since part of the disk experiences a higher inflow velocity. This effect appears both for horizontal shear (maximum value 1.24) and vertical shear (maximum value 1.30).

In the uniform-flow case, the profiles are symmetric with respect to the propeller axis; this is not the case for the shear-flow condition, where the side of the disk exposed to the higher incoming velocity exhibits a larger induced velocity, producing an asymmetry in the velocity field.

The radial mean velocity is also analyzed in Figure 22 (right), measured at the same axial location. In the uniform-flow case, this quantity starts from a positive value near the hub and the blade root and then decreases as the radial position approaches the tip. Under shear-flow conditions, the radial velocity becomes predominantly negative, with pronounced peaks near the mid-span region of the blade.

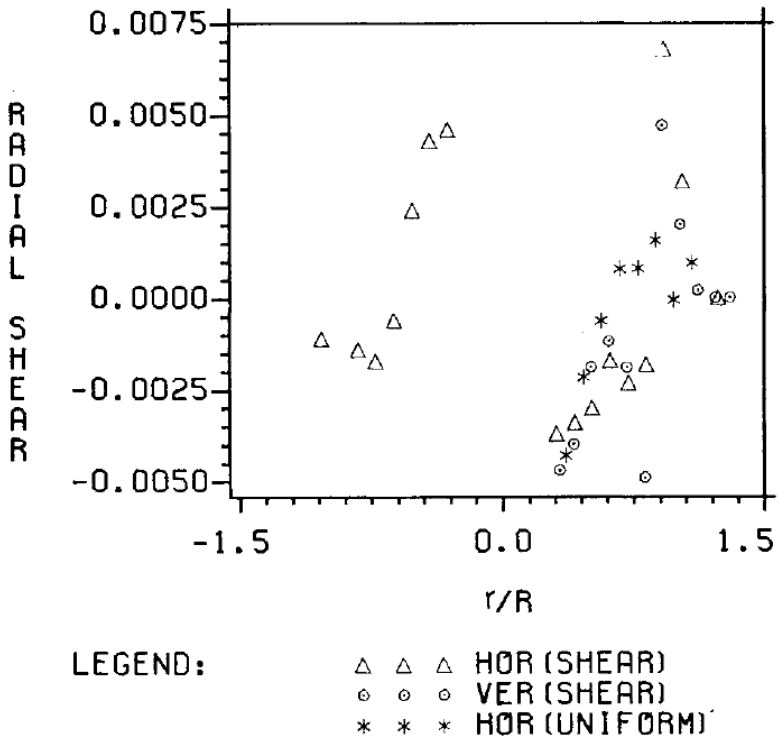

Figure 23: Reynolds stresses, $(u'v')$ [8].

Significant results also emerge regarding turbulence. Figure 23 reports the values of the radial Reynolds stress $u\prime v\prime$: in the uniform-flow case, the maximum is approximately 1.5×10^{-3}, whereas in the shear-flow case substantially higher peaks are observed, reaching values of about 7×10^{-3}(i.e., 400–500 of the uniform case). Here as well, the stress is negative near the propeller hub and increases toward the blade tip, eventually becoming positive. These behaviors are consistent with the formation of two vortical structures: a tip vortex and a trailing vortex sheet.

The figure also shows that, in the shear-flow case, the curve is vertically shifted, displaying an asymmetry in the peak values: with this combination of propeller operating conditions and shear inflow, the propeller exhibits higher Reynolds stresses near the blade hub than near the tip.

In the existing literature, several flow conditions have been investigated, each characterized by specific features and exhibiting different effects on the propeller aerodynamics and its operation; as shown, these effects can also be significant. In the present work, the shear-flow condition is selected for analysis, in a flow configuration similar to that proposed in Kotz's study, but with the thrust oriented in the opposite direction and employing different measurement techniques. The analysis focuses on two main aspects:

- Aerodynamic performance and loads: thrust and torque are evaluated, together with any additional relevant aerodynamic forces and moments;
- Wake: velocity fields within the propeller wake are measured and the turbulence characteristics are analysed.

Part III.
Instrumentation and measurement chain

The current part is divided into two sections: a first section is devoted to the analysis of each individual component used during the testing campaign, focusing on major interest components, while the second section is dedicated to the description of the test and its measurement chain.

Components and instruments of the experimental system

Windshaper facility

Figure 24: Windshaper facility [9].

The Windshaper is a multi-fan wind generator, main element of the testing campaign.

The WindShape technology aims to develop a real wind and weather simulator (Noca et al. [10]), mainly designed for testing flying vehicles in controllable atmospheric conditions. Windshaper facilities are completely modular and thus can be assembled into different geometries to meet a wide variety of experimental needs. This facility consists of small fans called “wind pixels”, each with independent control capability. This type of configuration has two main advantages:

- Allows broad control over generated wind properties, which cannot be replicated in conventional wind tunnels except through ad hoc devices;
- Small size fans has low inertia, allowing rapid changes in wind speed.

A wind generator unit composed by 9 wind pixels is called "wind module". These modules characterize the geometry of the Windshaper, allowing the component to generate variant wind in time and space. A Windshaper equipped with 48 modules was used for the experimental campaign, with a rectangular configuration of 8 modules horizontally and 6 modules vertically, for a size of about 2 x 1.50 m. A special interface allows control of the modules, by power percentage: it is possible either to choose a specific power percentage and vary it manually or to impose a power variation law in space or time. It is also possible to control the Windshaper via MATLAB using Python 3 API.

Since the Windshaper is controlled by power percentage, it becomes necessary to perform a calibration of the component, through the use of the five hole probe.

Five Hole Probe

The five hole probe is an improvement of the two-hole Conrad and three-hole Cobra probes (Saikiran et al. [11]). This type of probe has precisely 5 holes, 4 of which are placed in the left, right, up and down positions and one placed in front of the flow that allows the stagnation pressure to be measured. Through the 4 perpendicular holes, it is possible to acquire the direction of the flow knowing the pressures: thus, it is possible to fully indicate the pressure and velocity fields.

This type of instrumentation is extremely important in the present case study, as we want to analyze and characterize a three-dimensional flow coming out of the Windshaper: therefore, it is also necessary to know the pitch and yaw angles of the flow in order to take full advantage of this facility's ability to develop variant space-time flows, as well as for the calibration of the Windshaper itself.

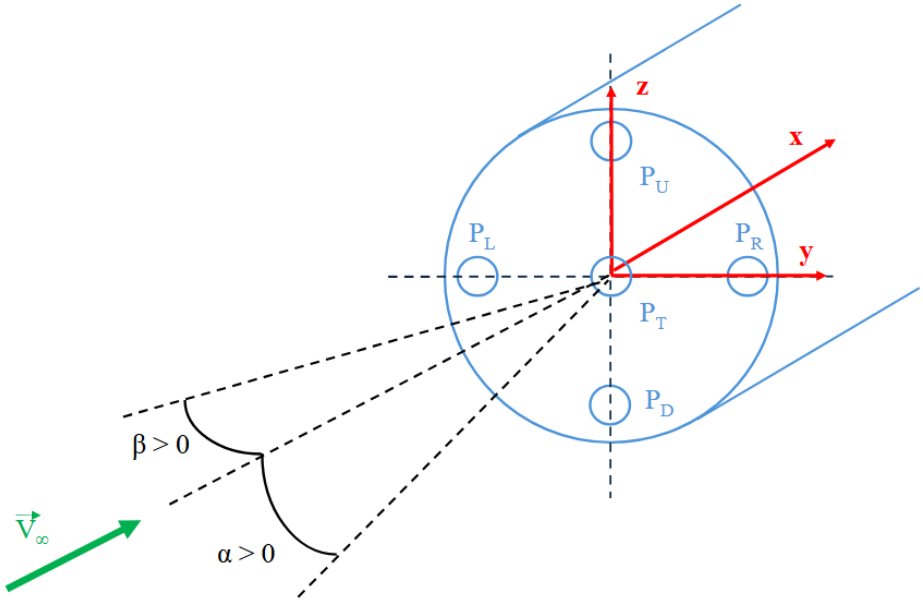

Figure 25: Schematic representation of the five hole probe.

They are then defined as:

- P_U and P_D, directional inlets in the vertical X-Z plane, sensitive to angle α;
- P_L and P_R, directional inlets in the horizontal X-Y plane, sensitive to angle β;
- P_T, front inlet, which measures the total pressure for $\alpha \neq 0$, $\beta \neq 0$;
- P_M, average pressure, which can be defined as

$$P_M = \frac{1}{4}\left(P_U + P_D + P_L + P_R\right)$$

- q, dynamic pressure, calculated as $P_T - P_M$, therefore also measured by $\alpha \neq 0, \beta \neq 0$.
- q_{true} e $P_{T_{true}}$ are the dynamic pressure and total pressure measured at calibration with the probe aligned with the current, then $\alpha = 0, \beta = 0$.

The established sign convention: for $\alpha > 0$, $P_D > P_U$, for $\beta > 0$, $P_L > P_R$.

The five hole probes can be of different types. Each probe has a non-linear response influenced by various factors, including tip geometry, hole distance and size, and viscous effects. The probe requires calibration to correlate the response to different flow conditions.

Zaber Guide

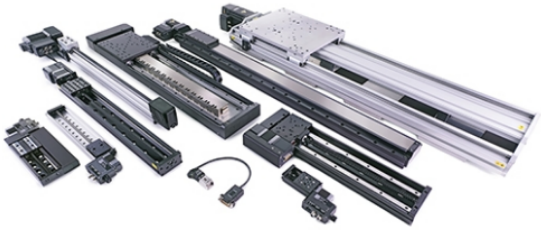

Figure 26: Some Zaber linear stages [12].

The Zaber Guide is a 3-axis automated system used during the experimental campaign to move the 5-hole probe in order to accomplish flow characterization. The guide is equipped with 3 linear stages, with travel length of about one meter for the y-axis, the longest, 540mm for the x-axis and 200mm for the z-axis. Handling accuracy is very high, down to the micrometer, and resolution down to the nanometer.

The guide can be moved either manually or automatically and has magnetic limiters to set the desired travel length: during the experiments, it was moved automatically using MATLAB scripts and Zaber dedicated software. The position and reference axis for Windshaper and Zaber Guide are represented in Figure 27.

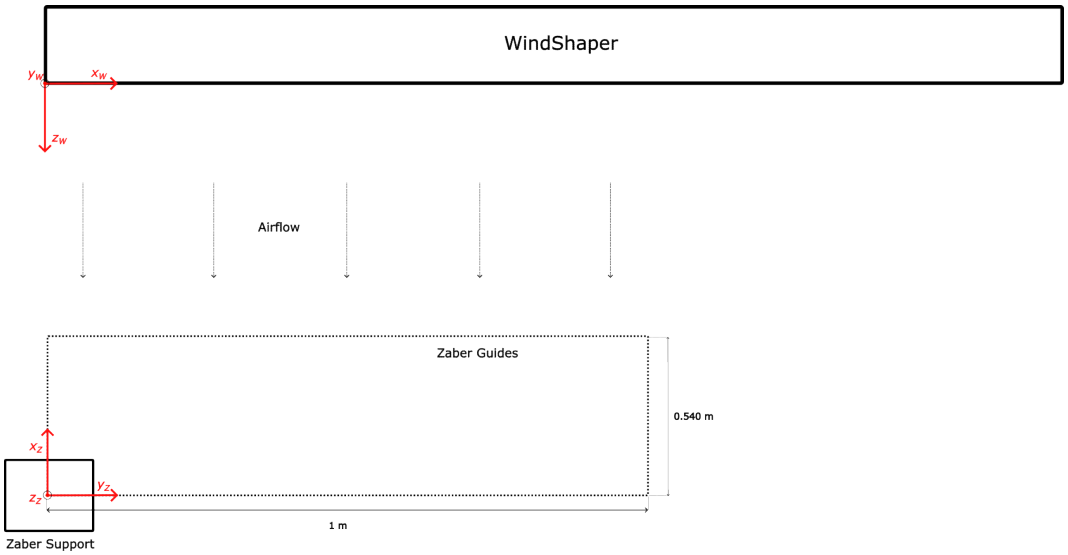

Figure 27: Position and reference axis, Windshaper and Zaber Guide.

Loading cell

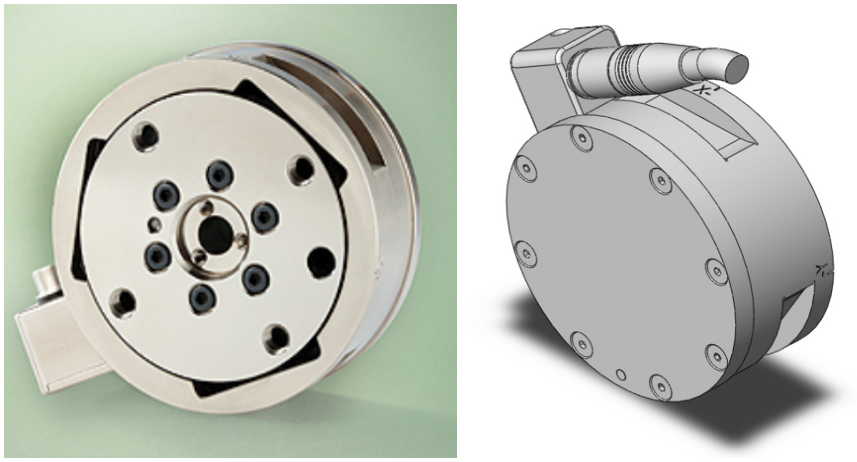

Figure 28: Gamma Transducer [13].

An F/T sensor Gamma load cell produced by ATI was used for the experimental campaign. Such a cell is called a strain-gauge cell; it consists of an elastic metal body equipped with strain gauges whose electrical resistance changes in response to strain. Specifically, an elongation of the strain gauge results in an increase in resistance and vice versa.

The cell's strain gauges are electrically connected in a configuration known as a Wheatstone bridge: this is a circuit of four resistive branches arranged in a rhombus shape, which provides a linear and accurate measurement as well as compensation for thermal effects. When force is applied, the cell body deforms, causing changes in the strain gauge resistances, which unbalances the bridge by generating an output voltage proportional to the applied force.

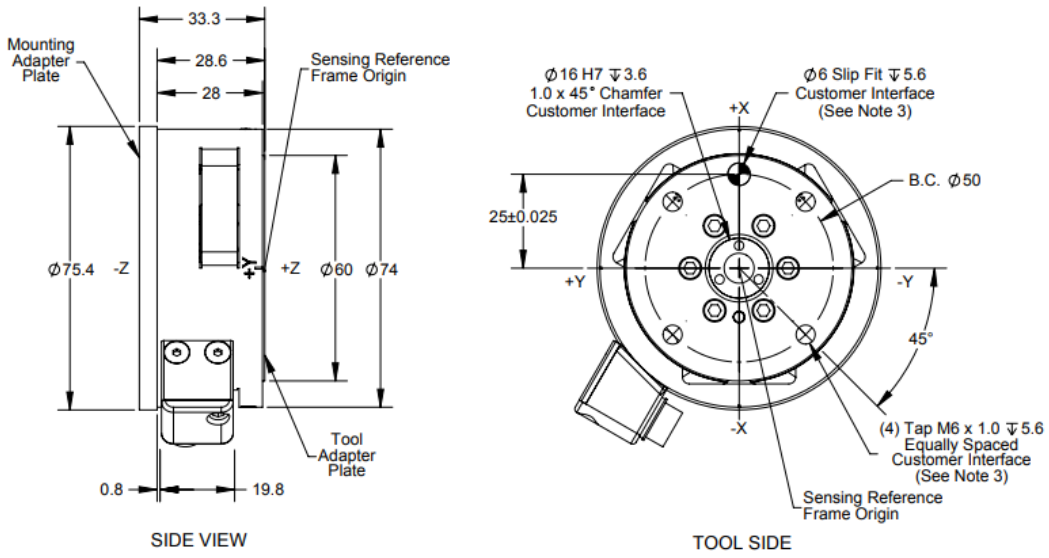

Figure 29: Technical drawings of the load cell [13].

In Figure 29, technical drawings of the load cell are shown, which are useful for observing component dimensions and reference axes. In Table 1, sensing range and resolution are

reported:

Calibration	F_x,F_y	F_z	T_x,T_y	T_z
SI-32-2.5	32 N	100 N	2.5 Nm	2.5 Nm
	Sensing ranges			
Calibration	F_x,F_y	F_z	T_x,T_y	T_z
SI-32-2.5	1/160 N	1/80 N	1/2000 Nm	1/2000 Nm
	Resolution			

Table 1: Metric calibrations (SI).

Particle Image Velocimetry

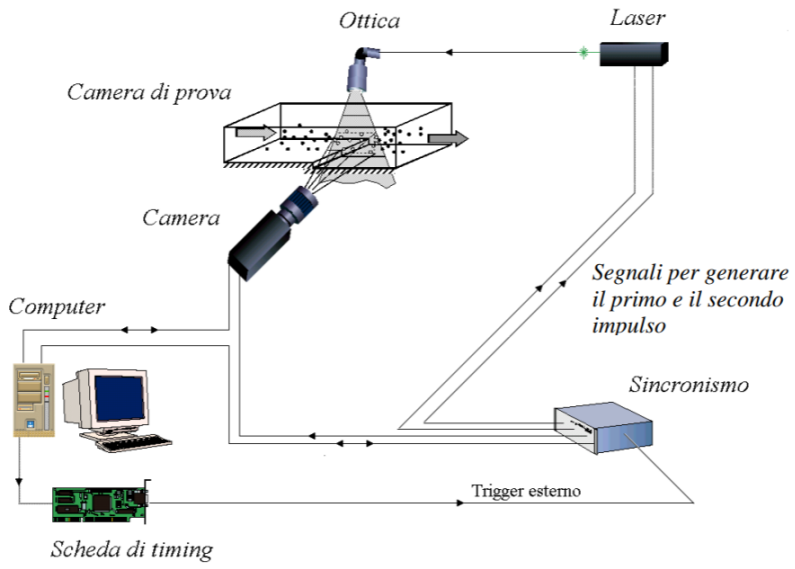

Figure 30: Diagram of a generical PIV setup.

Particle Image Velocimetry (PIV) is a non-invasive optical technique, suitable for evaluating instantaneous velocity field, that has been used to characterize the propeller wake.

In particular, in this case, the 2D2C planar PIV configuration was used, which allows the velocity field to be evaluated in a plane, captured by a camera: there will therefore be two velocity components. The accuracy of the measurement, defined as the number of velocity vectors detected, depends on the spatial resolution of the camera.

This type of technique involves introducing particles into a flow, which are then illuminated by a laser beam in the domain of interest. A camera then takes two snapshots in rapid sequence in order to visualize the illuminated particles.

The velocity at each point is evaluated by defining the velocity

$$v = \frac{\Delta s}{\Delta t}$$

Once the snapshots have been acquired, the displacement of the particles is evaluated using special algorithms and the instantaneous velocity vector is then derived, by magnitude, direction and orientation.

This technique provides high spatial resolution thanks to the characteristics of the camera and the dimensions of the field of view. As a result, the number of velocity vectors obtained per unit area is typically high, usually ranging from 10,000 to 150,000 vectors. The temporal resolution, i.e. the frequency response, on the other hand, is related to the characteristics of both the camera and the laser source used to illuminate the particles and can therefore be very variable depending on the setup. In general, the main strength of the technique is its high spatial resolution, which enables accurate and non-intrusive measurement of the velocity field. This advantage, however, comes at the cost of expensive equipment and a complex setup that includes seeding the flow with particles that must faithfully follow the motion.

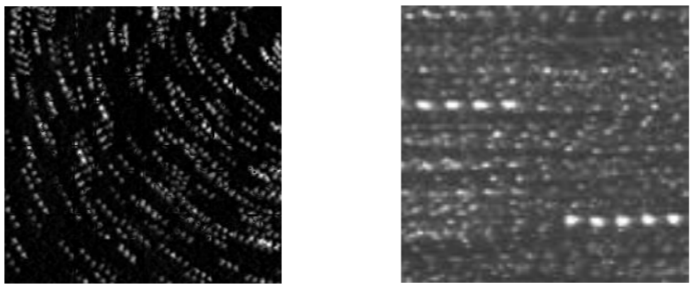

Figure 31: Example of PIV images.

PIV images appear as a black background dotted with white dots, the illuminated particles, as shown in Figure 31. It is important to keep the laboratory as dark as possible to avoid background noise in the measurement. There must also be a synchronisation system between camera and laser source, so that the snapshot acquisition and field illumination are coordinated.

In addition to autocorrelation or cross-correlation algorithms to evaluate displacements, a calibration to evaluate the difference between the displacement in the image plane and the physical plane is also necessary when analysing PIV images. So, the parameter M, magnification factor, has to evaluated:

$$M = \frac{\Delta L_{true}}{\Delta L_{image}}$$

Experimental setups and test protocols

Windshaper calibration and flow characterization

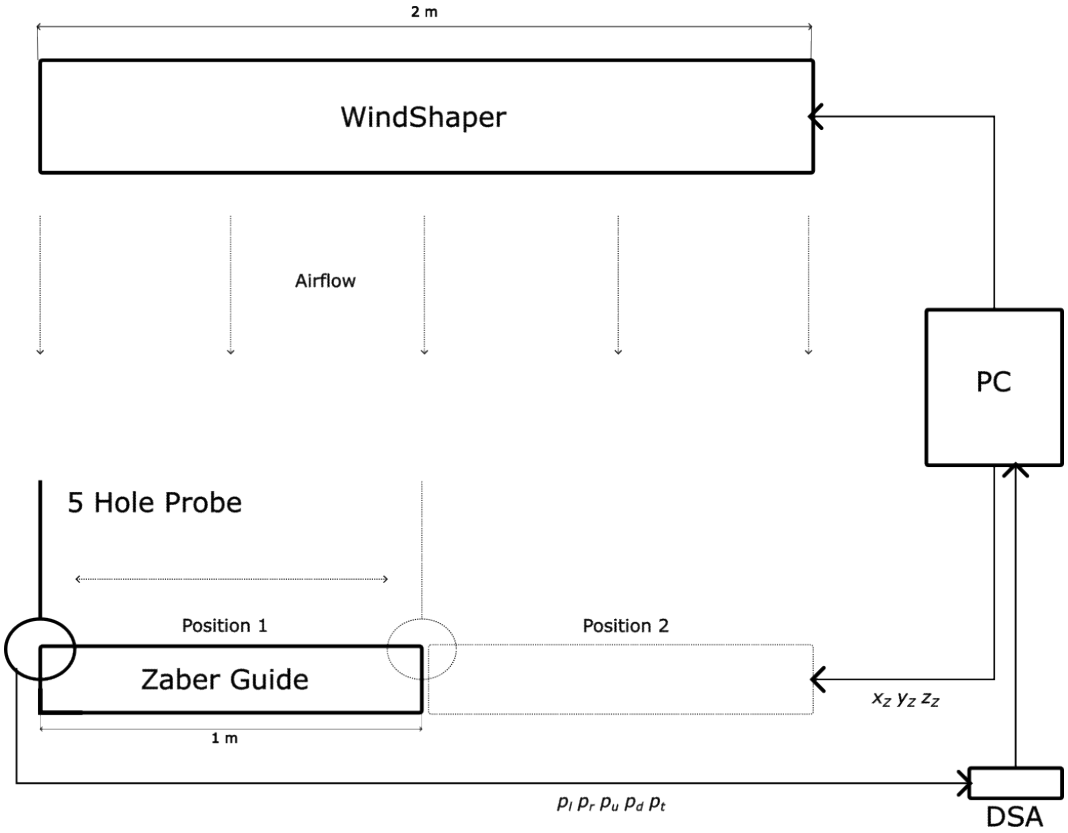

Figure 32: Block diagram - Windshaper calibration and flow characterization.

The first steps in the experimental campaign were calibration of the Windshaper and characterization of the velocity field generated by the component. The experimental setup used is shown in Figure 32 and is the same for both tests.

The Windshaper calibration was performed by keeping the probe stationary on the guide, with tracking on the central point of the generated flow: pressure samples were then collected while holding the Windshaper running at various power percentages, and the linear interpolation curve was then plotted. The pressure data coming out of the 5-hole probe were digitized using a component called the Digital Sensor Array (DSA), a pressure scanner manufactured by the Scanivalve company ([14]). It is a stand-alone pressure scanner, capable of processing up to 16 pneumatic inputs, suitable for cases where long calibration intervals and high accuracy are needed. The component contains 16 pressure sensors, an A/D converter and a microprocessor.

Figure 33: Digital Sensor Array [14].

The connection to the DSA is handled through a Python script, which allows the device to be controlled and pressure data to be acquired, then entered into the MATLAB environment where it is postprocessed. In the present case, five pressure ports plus the weather port are used.

The experimental setup allows the conditions of a flow to be analyzed point by point, producing the following output:

- The X-Y-Z coordinates relative to the measurement, defined in the Zaber reference system;
- A value f indicating the frequency in Hertz at which the measurement was taken;
- A struct named "data" which contains the values of the static pressure in the 4 directions and the total pressure.

Acquisition of forces acting on the propeller - Shear flow

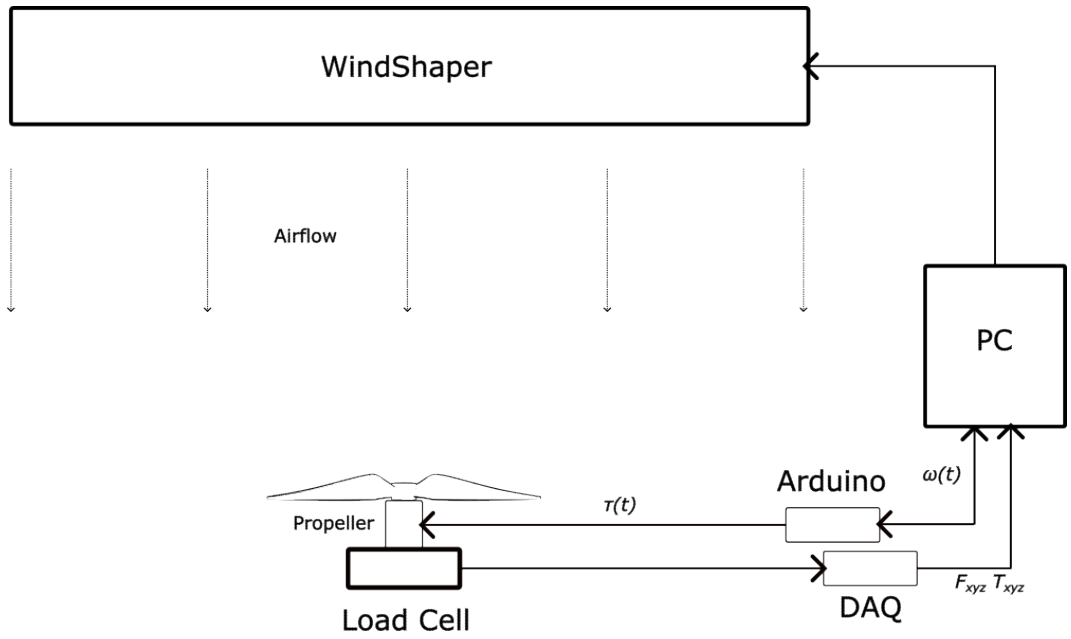

Figure 34: Block diagram - Forces acquisition, second setup.

This experimental setup shown in Figure 34 is used to measure the forces acting on the propeller under various conditions. The propeller system is mounted on the load cell via 3D-printed interfaces made of Polylactic Acid (PLA) and is positioned at a height of approximately $1.40m$ and $1.50m$ from the Windshaper. The centre of the propeller is therefore positioned in such a way as to be contained in the flow, at a latidudinal distance of $1m$ (centre of the Windshaper) and approximately $0.60m$ vertical distance. The propeller is set in motion by an electric motor, which is controlled on the bench via an Arduino controller: the RPM number fluctuates from the nominal value ($2500RPM$ for most of the tests), with oscillations of approx. $\pm 80RPM$ (3.2% of accuracy).

Both acquisition of forces and characterisation of the propeller wake were carried by means of the benchmark blade defined by Casalino et al. [15]: a $D = 0.3m$ diameter blade, derived from a two-bladed APC-96 model reshaping every single profile with NACA4412 airfoil. The profile starts at radius $1cm$ with an elliptical root section.

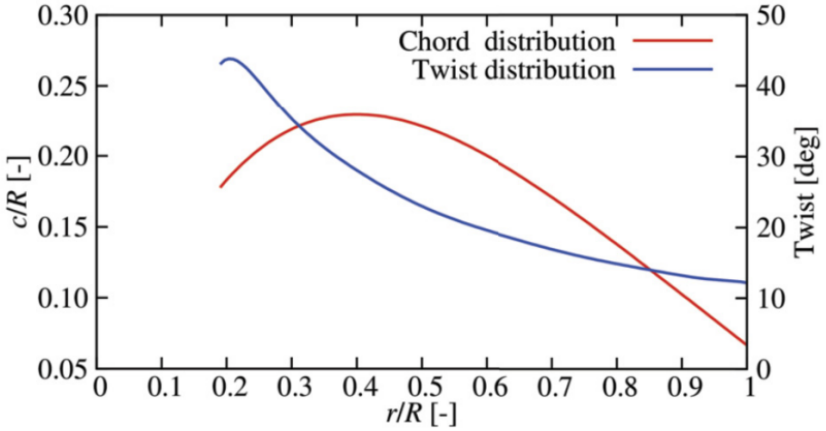

Figure 35: Blade chord and twist distribution [15].

This blade is mounted to an AT3520 Long Shaft Fixed Wing UAV Motor from T-Motor. The propeller is driven by an electric motor controlled by an Electronic Speed Controller system: this system manages signals generated by an Arduino, which implements a PID (Proportional-Integral-Derivative) control law, i.e. a regulation technique that consists of maintaining a physical quantity constant at a certain value (in this case, the RPM). The output is calculated as the sum of three terms

- Term P, proportional: this term responds proportionally to the measured error;
- Term I, integral: integrates the error over time to eliminate residuals;
- Term D, derivative: allows you to react to changes in error in order to dampen oscillations.

The control law will therefore be the sum of these terms:

$$\tau(t) = k_p \cdot e\,(t) + k_i \int e\,(t)\,dt + k_d \cdot \frac{de\,(t)}{dt}$$

Where $e\,(t) = \omega_{nom} - \omega\,(t)$. The value of $\omega\,(t)$ is returned by an RPM sensor integrated into the ESC system, while the ω_{nom} is the desired nominal speed. Set the constants k which define how the system reacts to the error, it is possible to calculate the output and therefore the motor command necessary to maintain ω_{nom}.

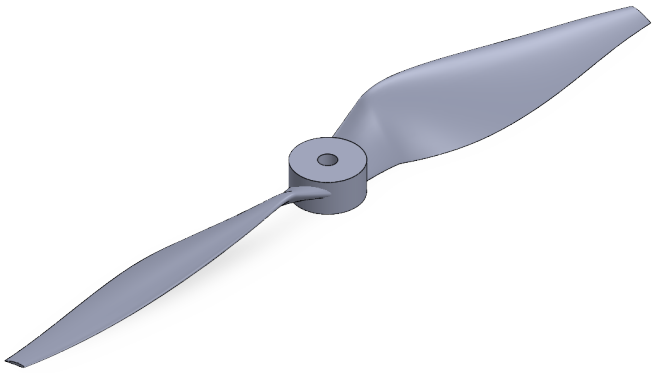

Figure 36: CAD of the propeller's blade.

The load cell is mounted at the rear and connected to a DAQ unit. The supplied voltages are then passed to the calibration matrix, which provides values for forces in N and torques in Nm.

Together with the main measurement of $120s$, two offsets of $30s$ are also acquired, one before and one after the main acquisition: this procedure is necessary in order to minimise the error on the measurement. The outputs therefore include

- 3 matrices, two containing the two offsets (150000×6) and one containing the main measurement (300000×6) where the columns represent in order the measurements of F_X, F_Y, F_Z and M_X, M_Y, M_Z;
- The T_{acq} value, acquisition time for the main measurement;
- The f value indicating the measurement frequency in Hz.

Characterization of the wake of the propeller

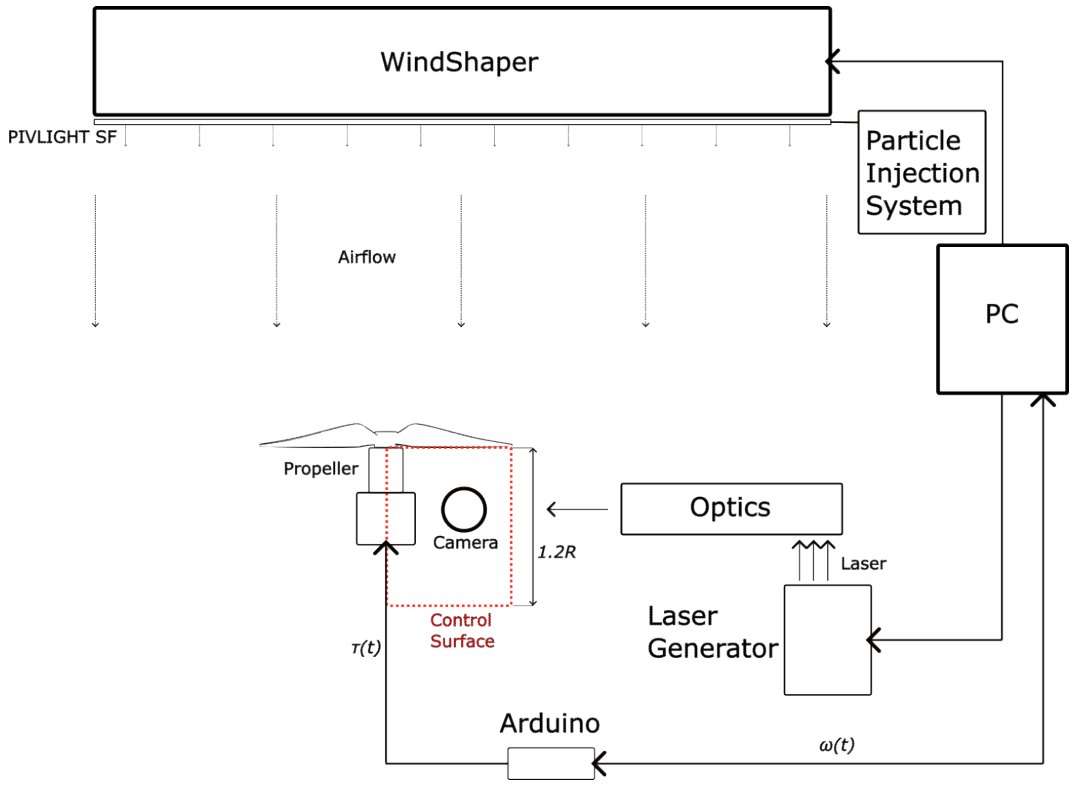

Figure 37: Block diagram - Wake characterization.

In this section, a completely different setup from the previous ones is presented, namely the PIV setup used for the propeller wake study.

For the PIV technique, it is necessary to seed the flow with reflective particles: in this case, PIVLIGHT seeding fluid particles sized $1\mu m$, atomised via a laskin nozzle, were used. These particles are injected downstream of the Windshaper fans through perforated tubes distributed along the fan array.

The data collection plane is an $x-y$ plane perpendicular to the Windshaper, positioned on the right rear side of the propeller-support system. Illumination is provided by a Litron Lasers laser, which generates a vertical beam ($z-axis$) that is mirrored and then passes through an optic that first concentrates it at one point and then expands it in the $x-y$ plane. This system is enclosed by a camera, a Nikkor AF 60mm, which shoots a scene $1.2 \cdot R$ long in the x-direction and R wide in the y-direction.

The laser operates in dual-pulse mode, emitting two pulses approximately 100µs apart at a frequency of $15Hz$. The camera is synchronised with the laser and captures two images with the same inter-pulse time and repetition rate. The total number of images taken at the end will be 4400 snapshots, resulting in 2200 calculated and analysed velocity fields. The output of this setup therefore consists of 4 matrices ($269 \times 319 \times 2200$), representing the fields:

- U: streamwise velocity, aligned with the propeller's rotation axis;
- V: radial velocity, directed towards the propeller's tip (W, not measured, is the out-of-plane velocity);

- ω: out-of-plane vorticity vector;
- $|V|$: magnitude of the velocity vector.

Vectors xx e yy are indicating positions in space.

Part IV.
Analisys of experimental results

Velocity field in front of Windshaper

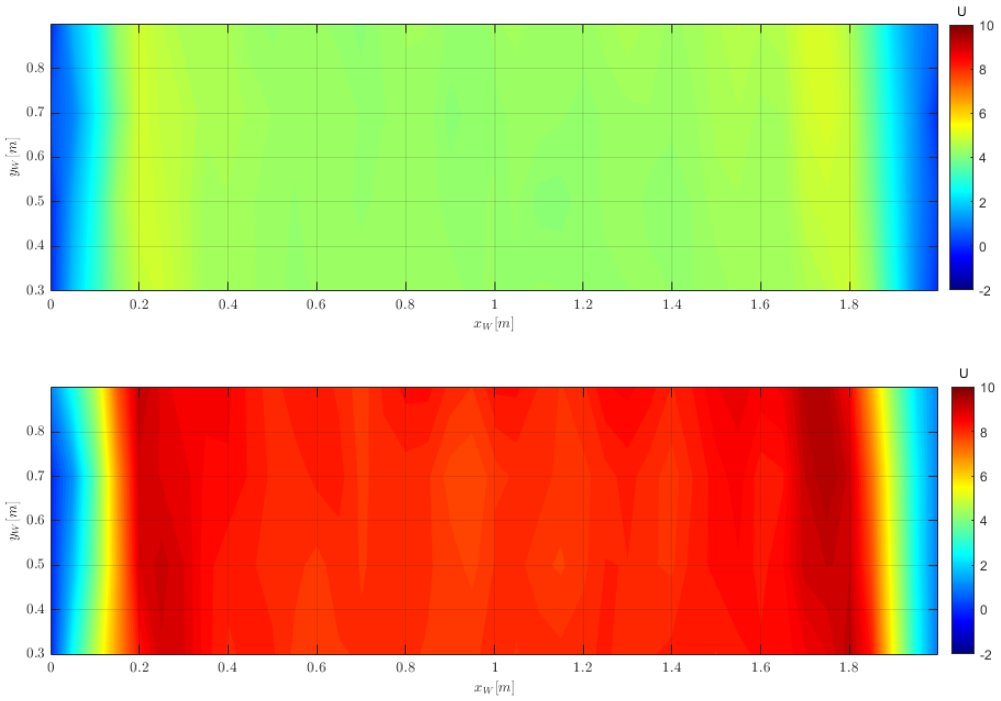

Figure 38: Velocity field for 25% and 50% of power.

The velocity field in front of the Windshaper was derived using the first experimental setup. The environmental conditions for pressure and temperature measurement are $p = 101325Pa$ and $T = 20°C$. The flow conditions were measured by taking 42 points horizontally (y-axis) and 4 vertically (z-axis) for a total of 168 points: The values of velocity U (along the x-axis) were then interpolated, and the field shown in Figure 38 was obtained. The results are shown for two Windshaper power settings and are consistent with the expected uniform-flow behaviour. At the limits of the measurement domain in the y direction, we can see that the velocity decreases, tending towards the steady state of still air. This does not occur at the limits of the field in the z direction, as the domain is more restricted in that direction and is therefore entirely contained within the flow.

For each point, the measurement time was approximately 2 minutes, for a total of 2000 samples acquired for each measurement point. The value displayed in the results is the average of the test results.

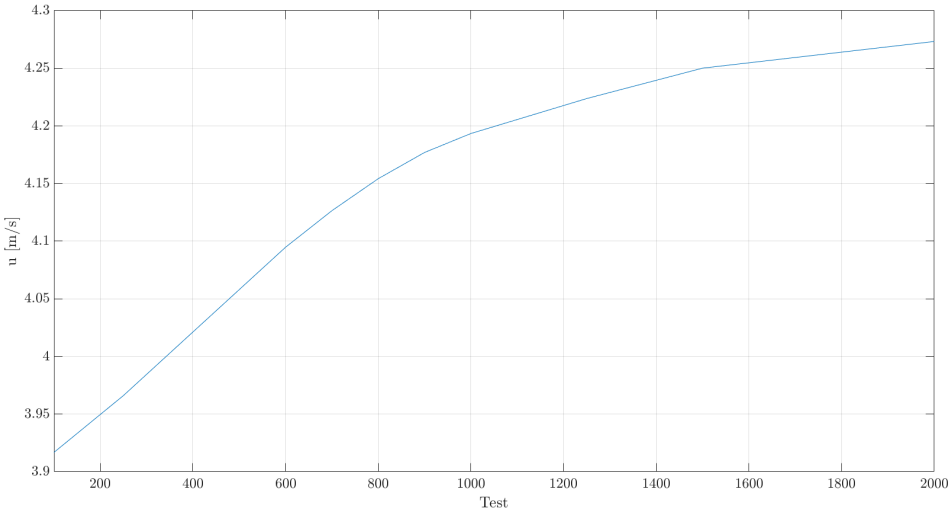

Figure 39: Convergence test.

In particular, the tests were analyzed separately, averaging the first n tests and comparing all the results. The curve in Figure 39 shows what has been described. The result tends to converge above 1200 acquisitions.

Propeller wake characterization

Study of the average field

The results of the PIV analysis were analysed in various ways, thanks to the more than 2000 velocity fields obtained through the test. One of these ways was to evaluate the mean fields obtained by Reynolds decomposition, i.e. to decompose the field into a mean component $\bar{q}$ and a component due to fluctuations q':

$$q = \bar{q} + q'$$

This section presents some of the results of this assumption, including mean velocity, vorticity and fluctuation fields.

Next, the velocity fields obtained using the PIV technique will be represented. These fields will always be displayed in the same mode: the graphs show the Control Surface depicted in Figure 40.

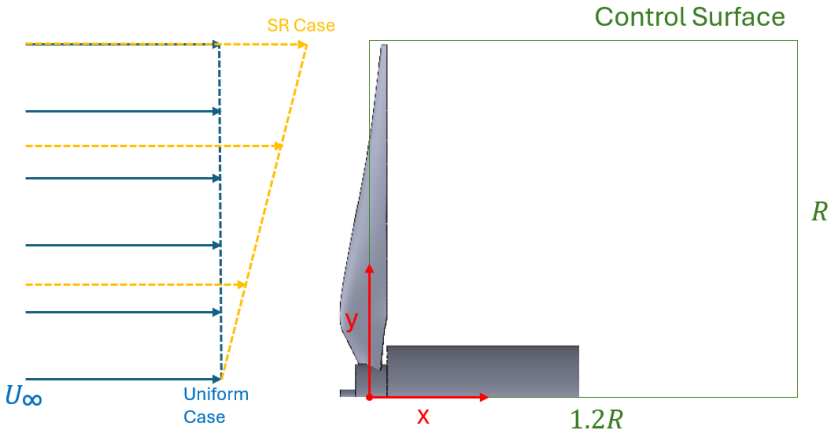

Figure 40: Visualisation of the velocity field downstream of the propeller.

For convenience, the various shear flow cases are indicated by the abbreviations SR. Defining $U_{ref} = U_\infty$ as the velocity at $(0, 0)$, Table 2 defines the SR case based on the velocity value U_{tip} that impacts the propeller at point $(0, R)$.

Case	$\Delta U = U_{tip} - U_{ref}$	$[\cdot]$
Uniform	0	m/s
SR1	0.5	m/s
SR2	0.75	m/s
SR3	1	m/s
SR4	1.5	m/s

Table 2: Shear Rate Cases.

Streamwise velocity

Here are presented the results of the wake characterisation. Various characteristics of the velocity field were analysed, starting with the streamwise U velocity.

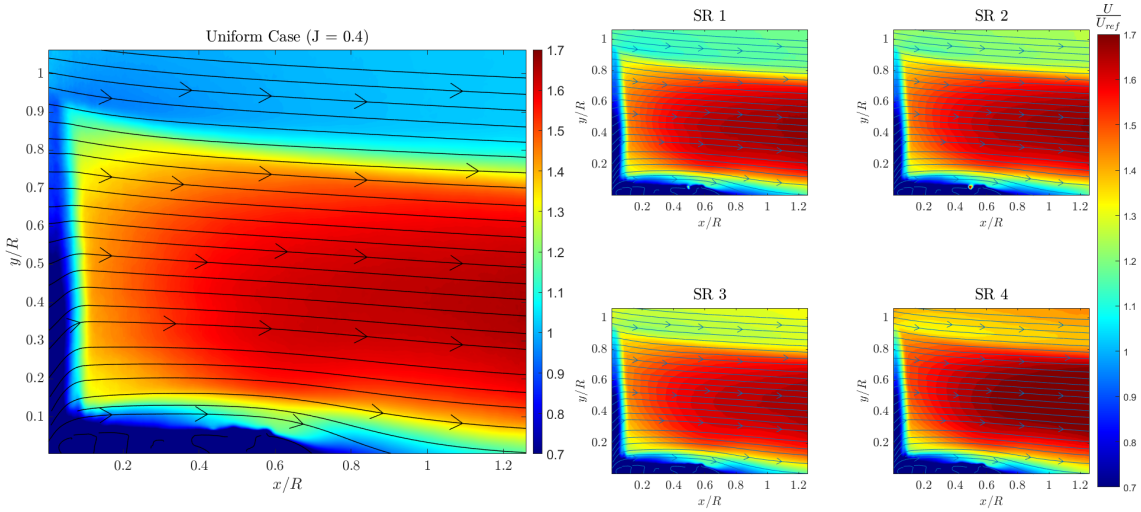

Figure 41: Normalised streamwise velocity U.

The velocity U is normalised by a reference velocity, i.e. velocity of the undisturbed inflow at the propeller hub: in the defined reference system, this point is located at coordinate $y/R = 0$. In this case, since $J = 0.4$, this velocity is

$$J = \frac{U_\infty}{N \cdot D} \Longrightarrow U_\infty \simeq 4m/s$$

Where $N = \frac{RPM}{60}$.

The space was instead normalised by the propeller blade radius $R = 0.15m$. The resulting velocity field visible within the Figure 41 clearly shows the behaviour of the wake, with the potential core shrinking as it moves away from the propeller in favour of the outer region at lower speed. A portion of the blade and engine, intercepted in the camera's field of view, are clearly visible, at the origin of the Control Surface.

The presence of shear flow produces some significant effects, including a radial expansion of the potential core and an increase in the streamwise velocities U detected within it. The outer region also has higher velocities. This behaviour was highlighted by studying the evolution of U along the y-axis by fixing two stations at two different x/R, the first near the propeller at a distance $x/R = 0.4$ and the second at a distance $x/R = 1$.

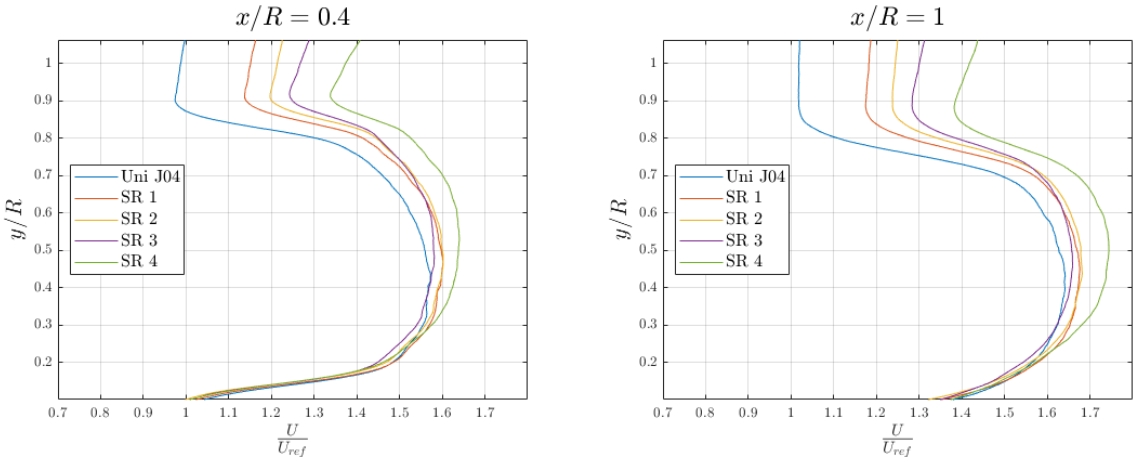

Figure 42: Normalised streamwise velocity component trend, fixed x/R.

Clearly, since the measurement plane is located in a region where the tangential velocity increases (from U_{ref} at $y/R = 0$ to U_{tip} at $y/R = 1$) the streamwise velocity profile U consistently shifts toward higher values as the imposed transverse shear rate (SR) increases.

Moving outside the potential core, for increasing values of U_{tip}, there is a tendency for the curve to 'flatten out', showing how at the transition to the outer region of the wake there are smaller velocity gradients and therefore higher U.

Radial velocity

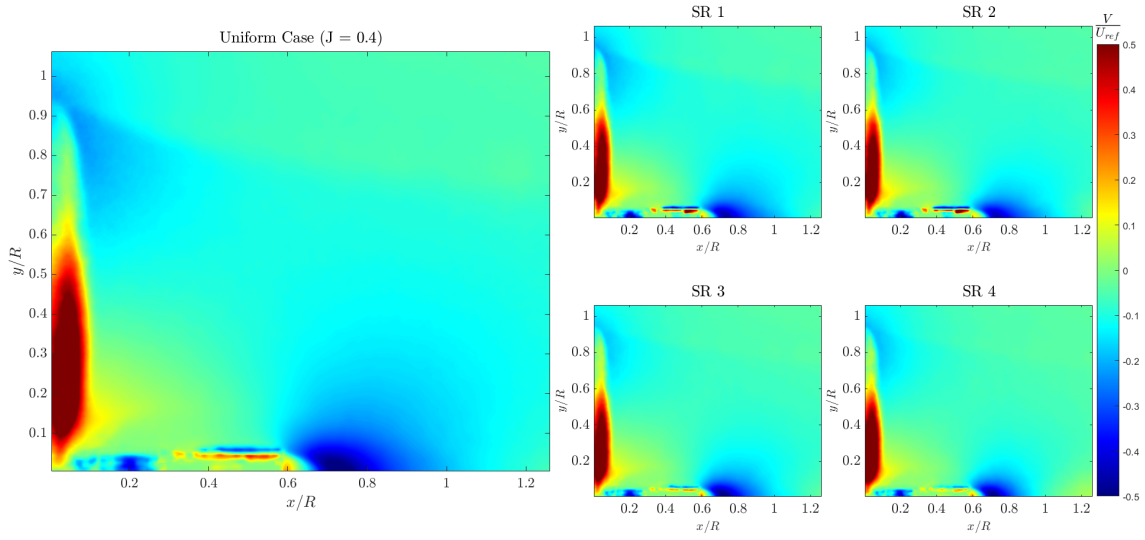

Figure 43: Normalised radial velocity V.

The radial velocity trend is analysed in Figure 43. Starting with the case of uniform flow, two main effects can be seen:

- The first effect is purely geometric: an increase in velocity is observed in the positive y-direction near the blade root, as the flow is diverted by the presence of the motor housing. The flow then follows the profile of the motor, explaining the negative velocity region present downstream of the component.

- The second effect is the presence of a region, at the tip of the propeller ($x/R = 0$, $y/R = 1$), where we can see a negative radial velocity: the flow through the propeller accelerates, so in order to respect mass conservation, the flow is drawn from the region outside the propeller. This therefore explains the velocity component mentioned above.

The presence of shear flow, in addition to the amplification of these two effects, also makes it possible to visualise the region where the tip vortex sheet is present, which presents a reduction compared to the negative value that characterises the region below: the vortex sheet is in fact characterised by positive and negative velocity fluctuations, which averaged over time provide the effect in the Figure.

Vorticity

This section presents the vorticity field, that describes the local rotation of the flow. It provides a measure of the intensity and distribution of rotational motion within the fluid and is particularly useful for identifying coherent structures such as vortices and shear layers in the wake. Vorticity is defined as

$$\omega = \nabla \times \vec{q} = \left(\frac{\partial v}{\partial x} - \frac{\partial u}{\partial y} \right) \hat{z}$$

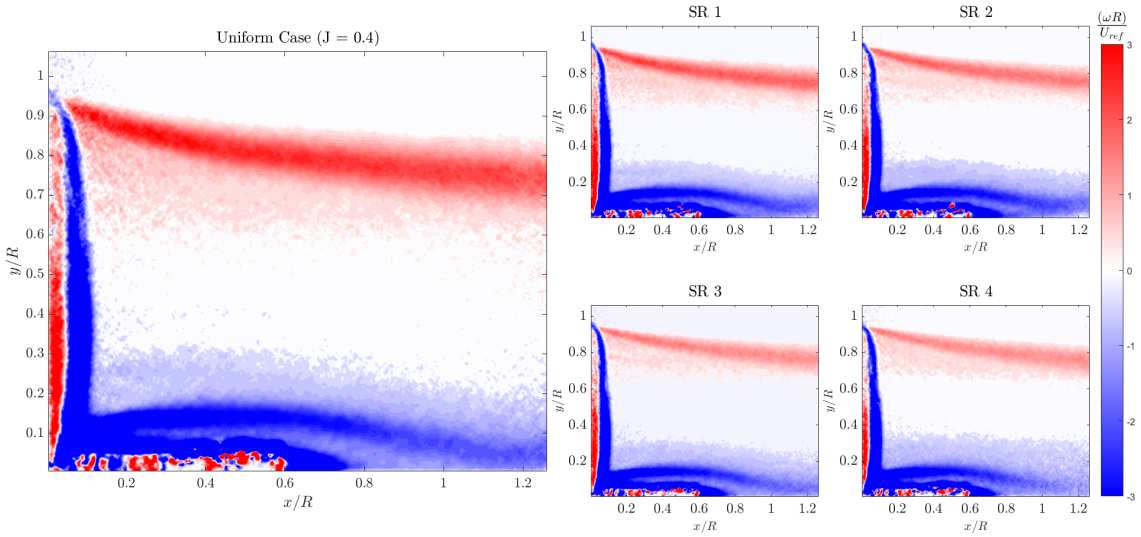

Figure 44: Normalised vorticity in the propeller wake.

Vorticity $[1/s]$ is normalised using the U_{ref} e R:

$$\frac{(\omega R)}{U_{ref}}$$

Two vortex structures are easily discernible in the Figure 44:

- The vortex structure at the top (from $y/R = 0.7$ to $y/R = 0.9$) is due to the tip vortices of the blade. These vortices, rotating counterclockwise ($\omega > 0$), detach themselves from the back of the blade and travel downstream.

- The second structure consists of trailing vortex sheets originating at the blade tip ($x/R = 0$, $y/R = 1$), convected along the blade edge (up to $x/R = 0$, $y/R = 0$) and around the engine housing, before detaching (around $x/R = 0.3$) and being transported downstream by the flow. These types of vortices rotate in the opposite direction to tip vortices, exhibiting negative vorticity.

Looking at the various vorticity fields obtained as the intensity of the shear flow varies, the behaviour of such structures becomes clearer when analysing the vorticity pattern radially instead, with fixed stations x/R and y/R. In this case, a moving mean with a window length of 20 was applied to eliminate background noise from the measurement.

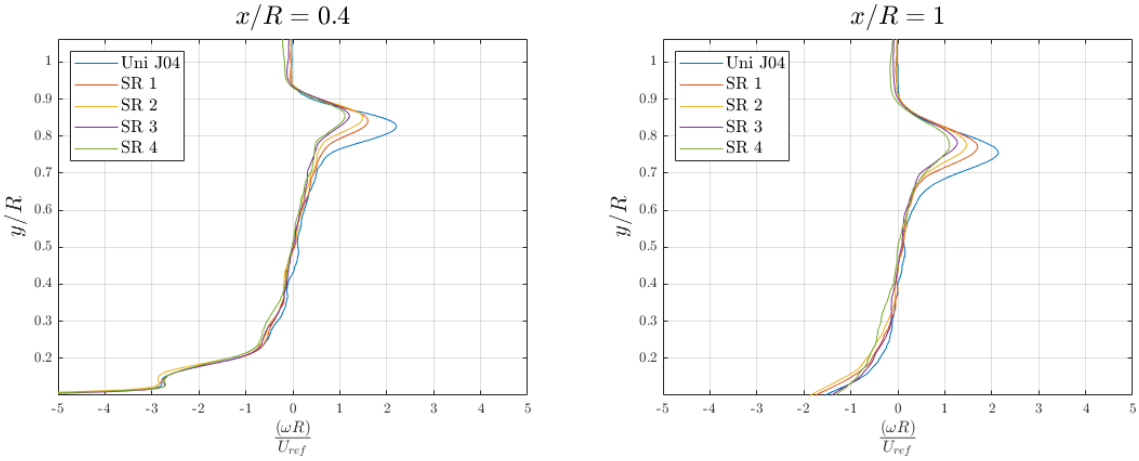

Figure 45: Normalised vorticity trend, fixed x/R.

It can be seen that as far as the trailing vortex sheet is concerned, there are no significant changes in behaviour, as this phenomenon is mainly dependent on the geometry of the blade and the motor. As far as tip vortex is concerned, on the other hand, there are two noticeable trends:

- Vorticity decreases in presence of the shear flow and as the shear rate increases: this phenomenon is related to the difference in speed between the suction side and pressure side of the blade, near the tip. This relative speed is decreased by the presence of shear flow, causing a decrease in lift at the tip and thus dampening tip vortex generation and lowering vorticity.

- Vorticity maxima move towards greater radial distances as the shear rate increases: vortices follow the flow, and are therefore transported outwards from the wake by the streamwise flow components that arise in the presence of shear flow.

Fluctuations and turbolent kinetic energy

Having averaged the velocity field, it is possible to go on to define the fluctuations

$$\overline{u'u'}, \overline{v'v'}, \overline{u'v'}$$

As part of the study of the Reynolds Averaged Navier Stokes (RANS) equations, these quantities are contained into the Reynolds tensor, the matrix that determines the effect of turbulent fluctuations on the Reynolds-mediated velocity field. Thus, these fluctuations

are also related to the turbulent kinetic energy κ: the behaviour of these fluctuation-related parameters has been represented here and then used to calculate the turbulent kinetic energy, minus the constant value ρ. Here, data are presented normalised for U_{ref}^2 and averaged using a moving mean with a window of length 20, to remove noise from the measurement.

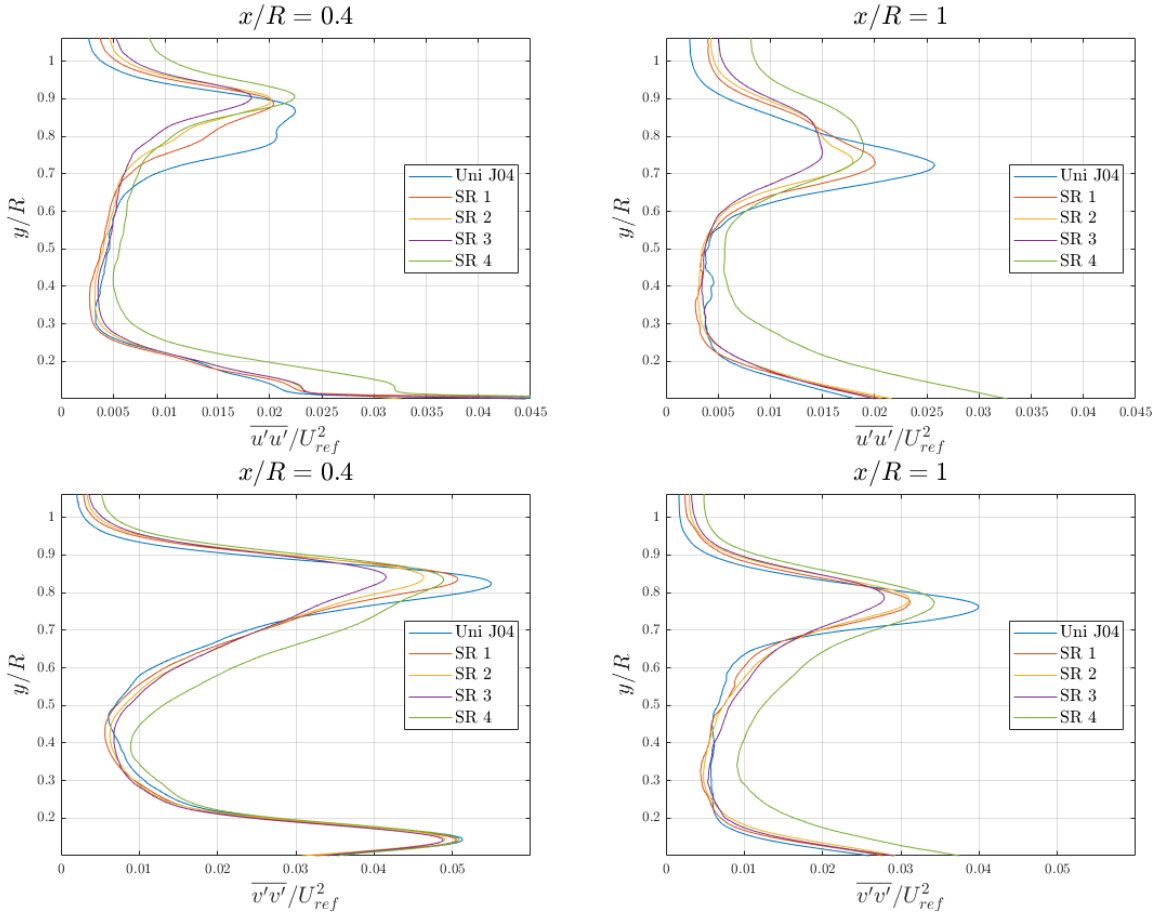

Figure 46: Turbolent fluctuations.

The trend of both parameters is similar for the uniform case, presenting peaks in the areas of higher vorticity. Moving on to the shear flow case, we can see how these fluctuations are damped for the blade tip region, while they tend to remain constant for the trailing vortex sheet, except for the last shear case where an increase is seen. We expect this trend to be present also in the turbulent kinetic energy analysis.

Turning to the analysis of the κ, this is defined minus the density as

$$\kappa = \frac{1}{2}\left(\overline{u'^2} + \overline{v'^2}\right)$$

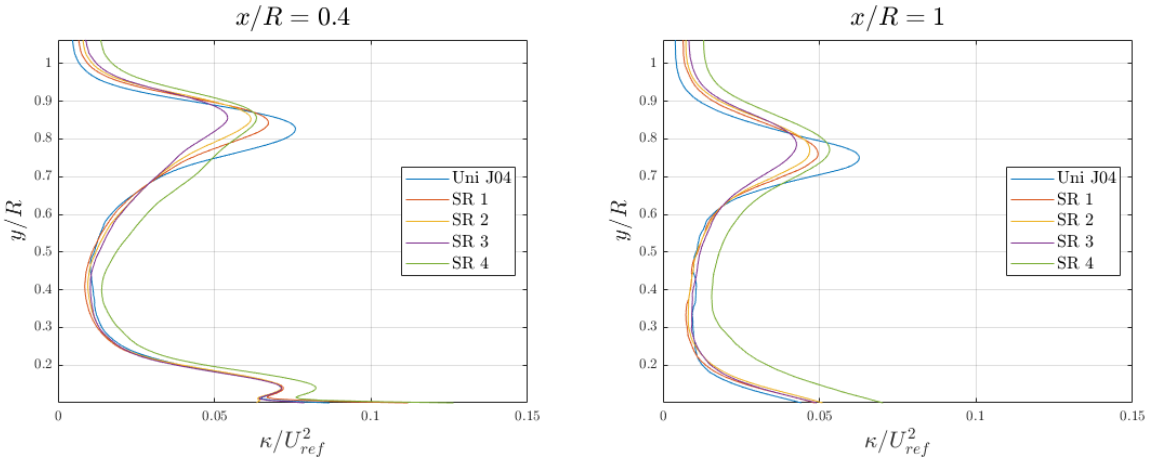

Figure 47: Normalised turbolent kinetic energy κ.

Again, as expected, in Figure 47 we see a reduction in κ from the uniform to the turbulent case in the tip zone and constancy in the zone crossed by the trailing vortex sheet.

Study of the phase average

In order to visualise the results more consistently, an analysis of in-phase averages was carried out. In particular, 36 in-phase averages were calculated considering "control sectors" of 5°: taking advantage of the symmetry of the problem, 180° phase-shifted fields were also added to these sectors in order to average over a greater number of velocity fields and thus obtain more accurate values.

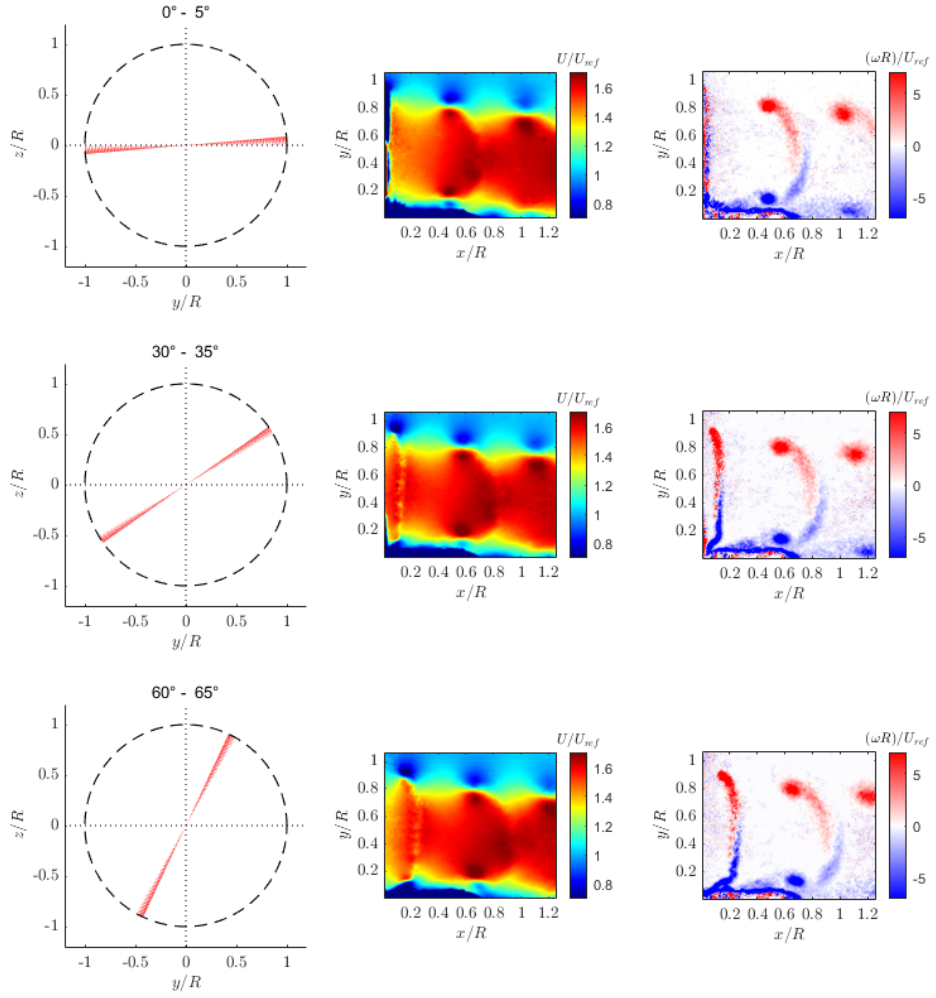

Figure 48: Uniform flow, first half: Blade sector, streamwise velocity U and vorticity ω compared.

What is obtained is the possibility of characterising the phase-averaged velocity field for all blade positions and observing the behaviour of the principal quantities. In a first representation in Figure 48, it is possible to identify a clear correspondence between the streamwise velocity and vorticity fields. The axis z is the vertical axis perpendicular to the plane $x - y$ of the Control Surface.

Streamwise velocity

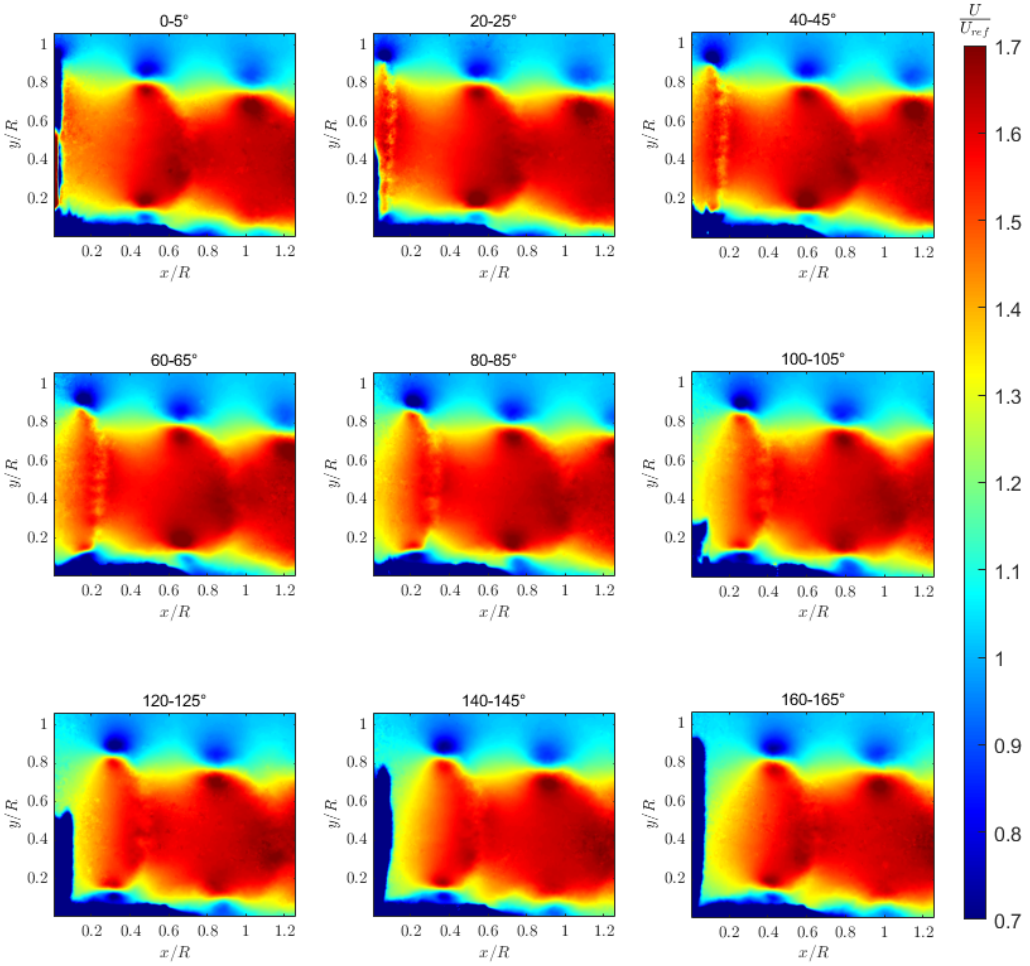

Figure 49: Streamwise phase-averaged velocity field, U.

In Figure 49, the evolution of the streamwise velocity field can be observed as the blade progresses through its azimuthal position. In this first representation it is possible to identify the vortex structures, in particular the tip vortex sheet already identified in the study of the averaged field is highly visible. Observing the Figure 49, it can be seen how the tip vortex detaches itself from the blade near the instant it crosses the horizontal position. The same applies to the trailing vortex sheet, identifiable as the small region at lower speed that forms along the blade in the early stages, and then disperses into the potential core around 120° degrees phase.

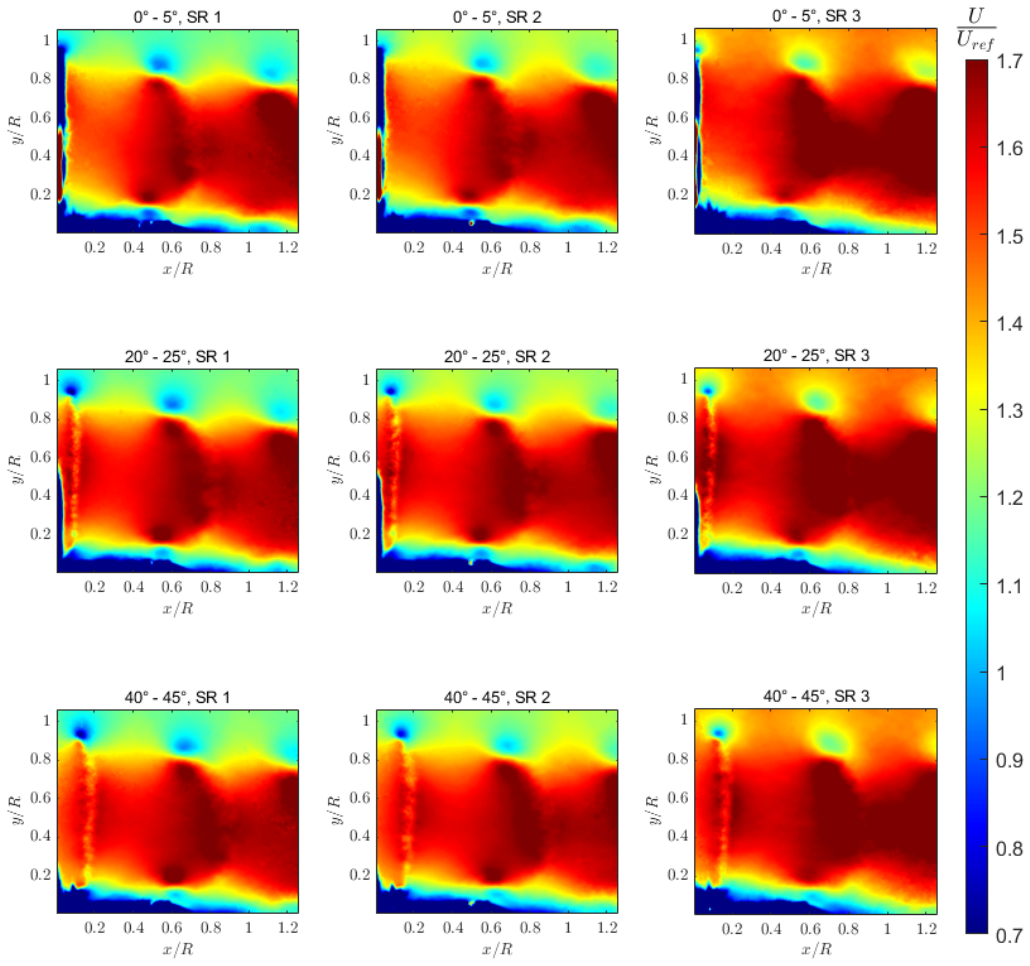

Figure 50: Streamwise velocity: influence of shear flow at three different phases.

In the analysis of the influence of the shear rate, the moments close to the passage of the blade are reported to capture the moment when the tip vortex detaches from the blade. In general, what happens as the shear rate increases is that the velocities within the vortex increase, both streamwise and radial velocity.

Vorticity

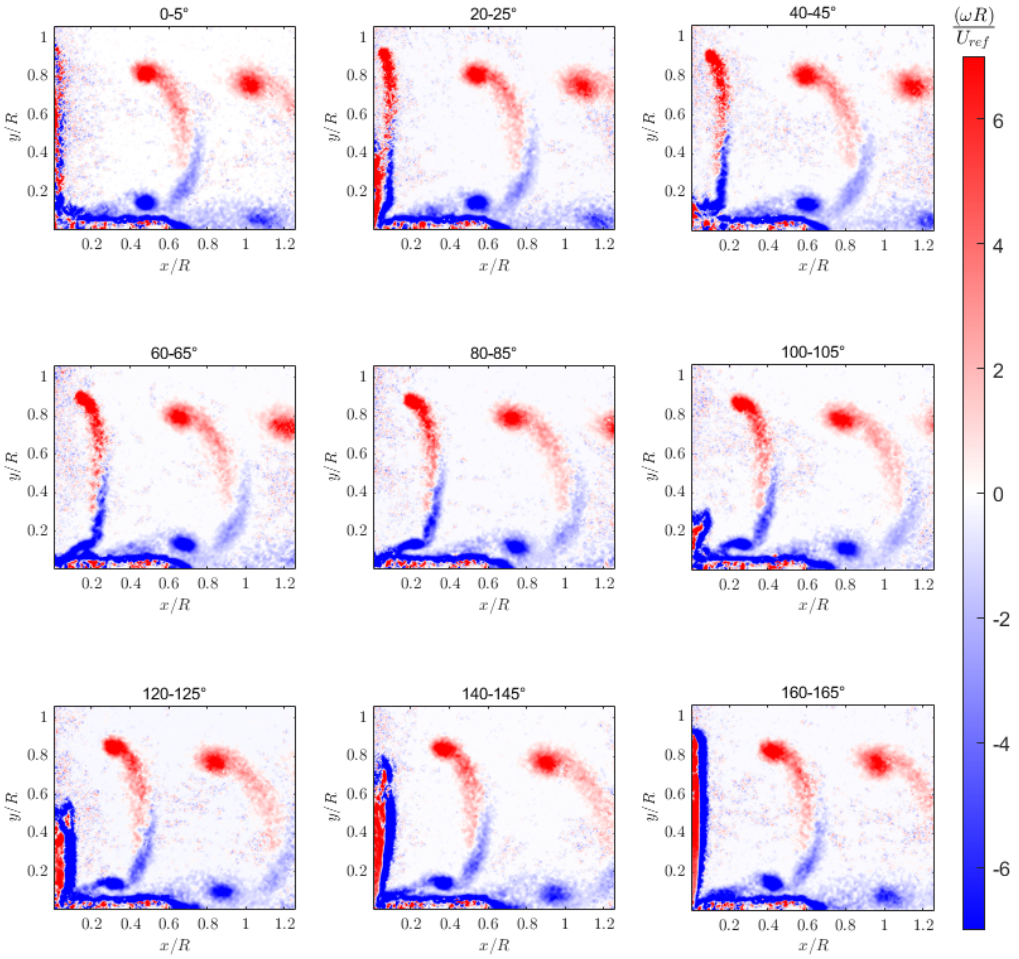

Figure 51: Normalised vorticity: phase-averaged field, ω.

This type of representation provides more indications with respect to the Reynolds-averaged vorticity field. In particular, it is possible to note the presence of an additional vorticity structure, due to the interaction with the motor body: this structure initially belongs to the trailing vortex sheet, and then detaches and evolves separately. In this case, the behaviour of the vortex structures already described in the previous sections, i.e. the detachment of the vortex as the blade passes, is clearly visible: however, in this type of analysis, the intensity, as well as the direction of rotation, of the structures is clearly visible, remaining consistent with the visualisations of U and V.

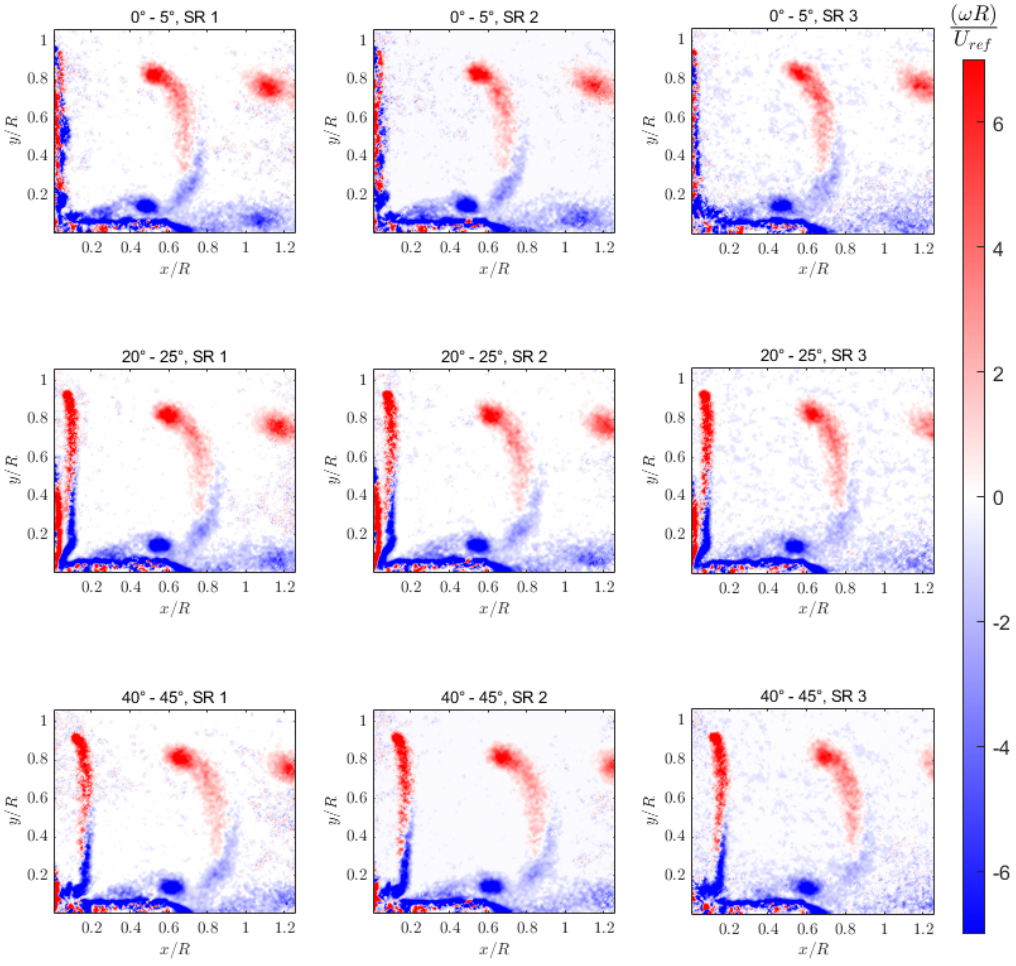

Figure 52: Vorticity: influence of shear flow at three different phases.

In this type of visualisation, make two observations:

- Vortices are transported faster downstream as the shear rate increases: in the previous analysis, where the field was Reynolds-averaged, it was not possible to identify this effect;
- Vortices are transported radially outward as the shear rate increases, as was already seen with the Reynolds decomposition.

From the vorticity maps shown in Figure 52, it is not easy to see the differences in the behaviour of the vortex structures: in this regard, the position of the centres of the tip vortices is analysed. In the maps, we can see the presence of three tip vortices: considering that two vortices are generated in one revolution, the third vortex relates to a previous revolution of the propeller and has not yet left the control surface.

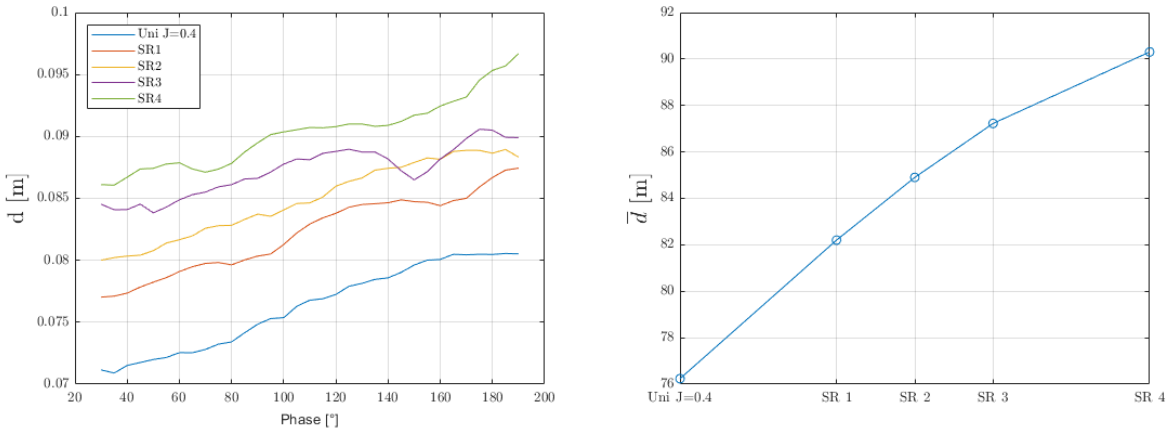

Figure 53: Streamwise distance of the centers of the tip vortices.

Analysing the data in Figure 53:

- On the left, the distances between the vortex centres (along x direction) are shown, starting from the moment when the second vortex relative to the revolution is fully formed (blade in phase of approximately 30°).
- On the right is the average distance between the centres of the vortices (along x) as the shear rate increases.

Both graphs confirm what has already been anticipated by displaying the vorticity map: as the shear rate increases, the vortices are further apart, thus confirming that they travel faster in the streamwise direction. In particular, both vortices undergo this effect, but the one further downstream is affected more, so the distance between the two vortices increases.

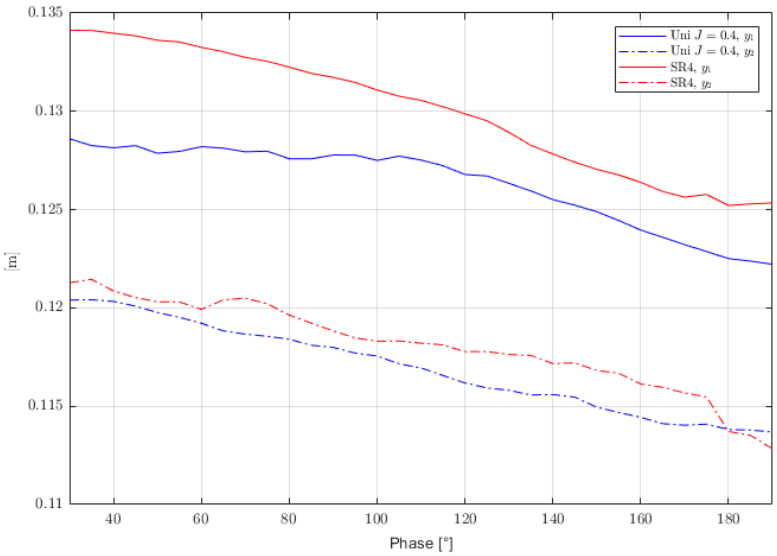

Figure 54: Effect of shear rate on radial position of the centers of the tip vortices.

This last graph in Figure 54 shows the trend of the radial coordinate of the vortex

centres. In the transition from the uniform case to the maximum shear rate case, both vortices are transported outwards. The vortex furthest from the propeller is most affected by this effect.

Triple decomposition

The aerodynamic contributions involved in the phenomenon under consideration can be further decomposed, taking into account the periodic effect on the flow due to the rotation of the propeller. The following triple decomposition is then performed:

$$u\left(x,t\right)=\bar{u}\left(x\right)+\widetilde{u}\left(x,t\right)+u''\left(x,t\right)$$

Where $\bar{u}$ represents the time average of the entire velocity field, while fluctuations u' are divided into two components:

- $\widetilde{u}\left(x,t\right)$represents the average velocity component in the u' fluctuations due to the phase;
- $u''(x,t)$ represents the purely stochastic component of velocity fluctuations.

In order to perform this triple decomposition, the velocity field $\widetilde{u}(x,t)$ was derived as

$$\widetilde{u}\left(x,t\right)=u_{phase}\left(x,t\right)-\bar{u}\left(x\right)$$

Where $u_{phase}\left(x,t\right)$ represents the phase average of the velocities analysed in the previous sections, with characteristic period τ:

$$u_{phase}\left(x,t\right)=\lim_{N\to\infty}=\frac{1}{N}\sum_{n=1}^{N}u\left(x,t+n\tau\right)$$

Phase-correlated component of fluctuations

Therefore, starting from the analysis of the velocity fields obtained from the PIV and comparing them with the results already analysed in the previous sections such as average field $\bar{u}(x)$ and phase-averaged $u_{phase}\left(x,t\right)$, it was possible to perform this decomposition and derive periodic components within the velocity fluctuations u'.

Therefore, based on the analysis of the PIV velocity fields and using both the time-averaged field $\bar{u}(x)$ and the phase-averaged field $u_{phase}\left(x,t\right)$, the triple decomposition was carried out. Then, $\tilde{u}$, $\tilde{v}$ and $\tilde{\omega}$ has been calculated.

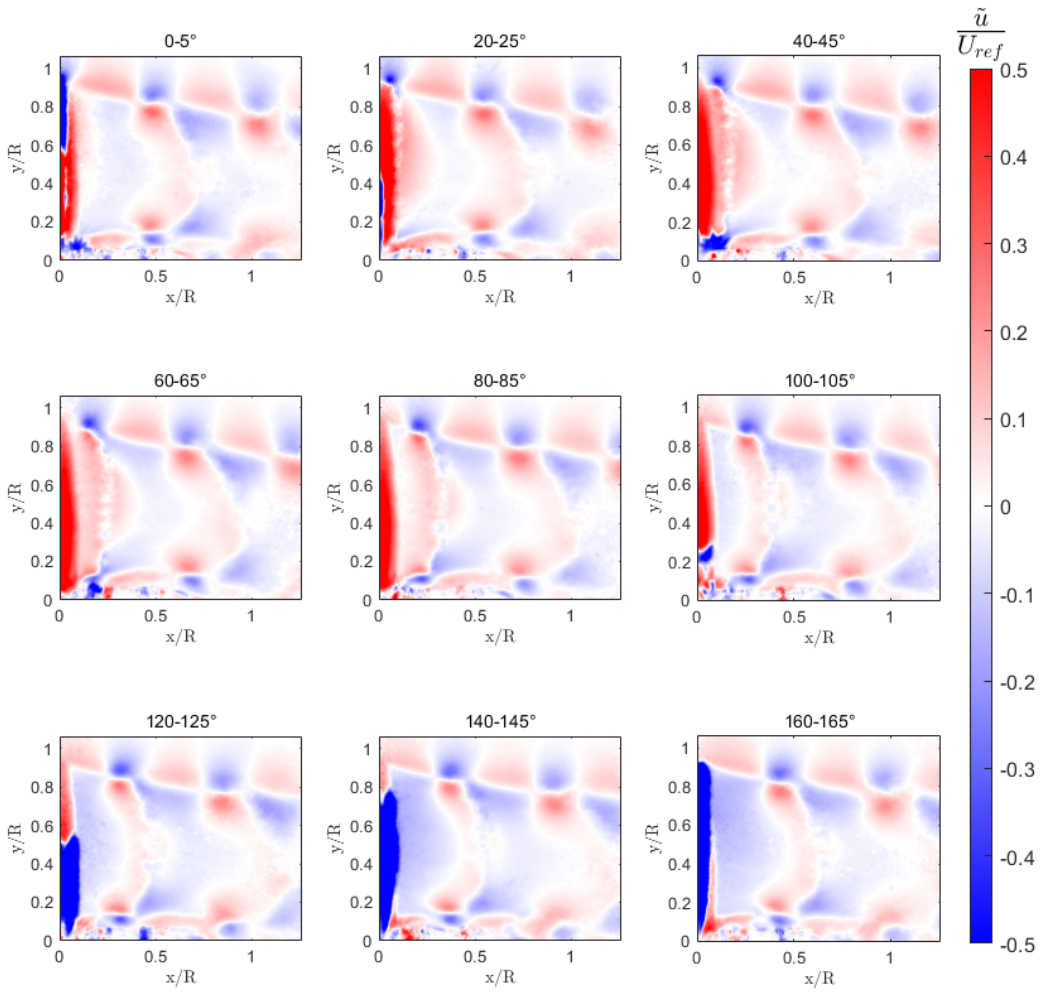

Figure 55: Streamwise periodic velocity components of fluctuations $\tilde{u}$, uniform flow.

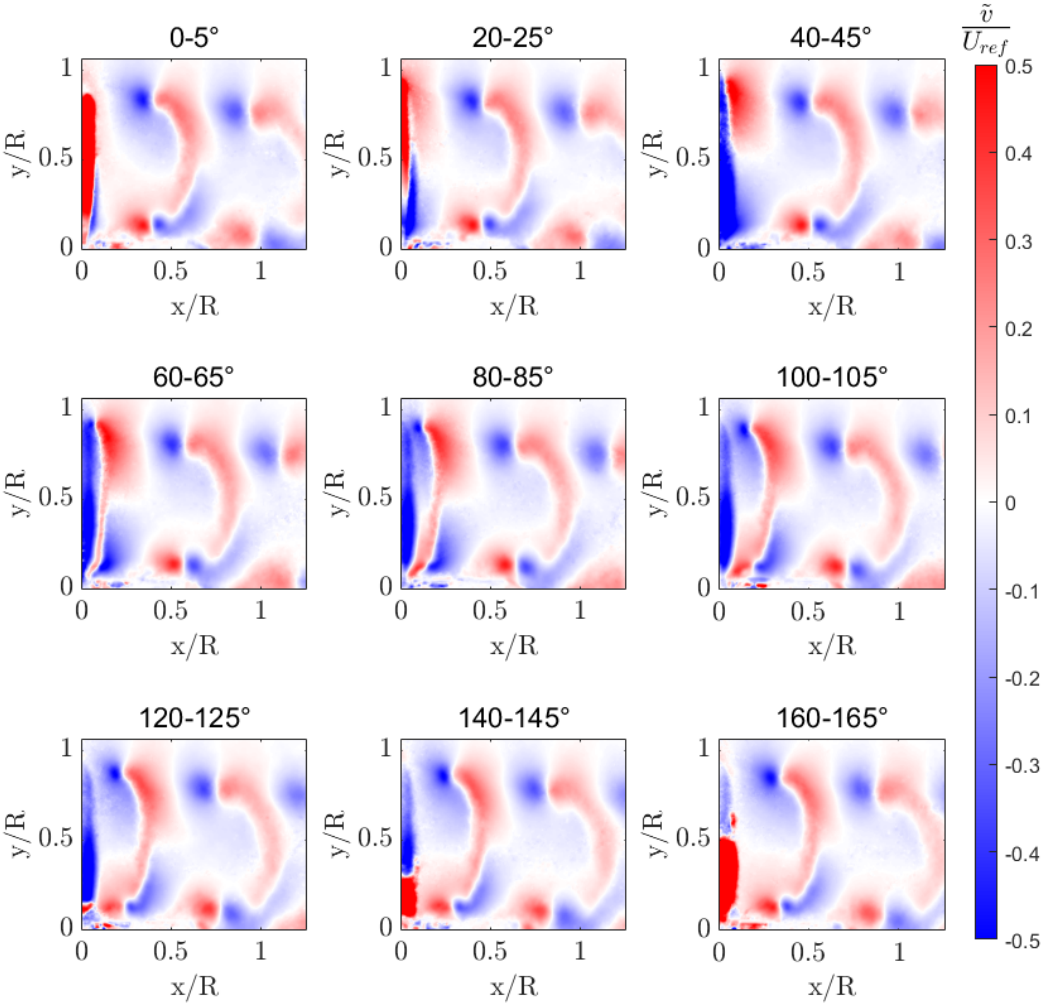

Figure 56: Radial periodic velocity components of fluctuations $\tilde{v}$, uniform flow.

The two Figures 55 and 56 shows the results, in uniform flow case, for streamwise and radial velocities. It is possible to recognise the contribution of the vortex structures generated by the rotation of the propeller, as well as the direction of rotation of these vortices and their evolution in time. Therefore, within the overall fluctuation field u', a significant deterministic and periodic component $\tilde{u}$ is present, directly associated with the propeller's rotational motion.

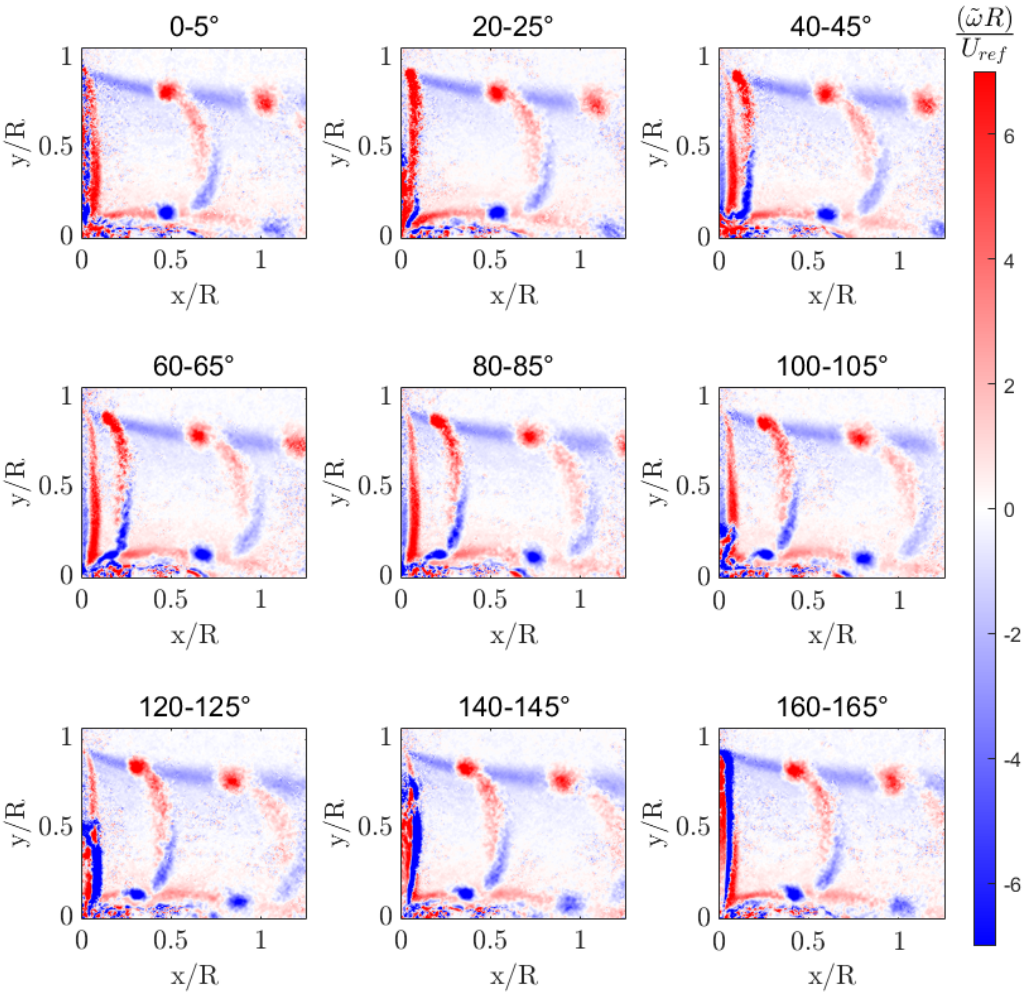

Figure 57: Periodic vorticity components of fluctuations $\tilde{\omega}$, uniform flow.

In addition, it is interesting to visualise the trend of $\tilde{\omega}$ in uniform flow case presented in Figure 57. This type of visualisation is the one that best enables the vortex structures to be identified. In fact, the three structures are perfectly distinguishable, namely the tip vortices, the vortex structure related to the interaction with the motor and the trailing vortex sheet, which is represented by the striations of vorticity that cross the Figure radially and evolve downstream decreasing in intensity.

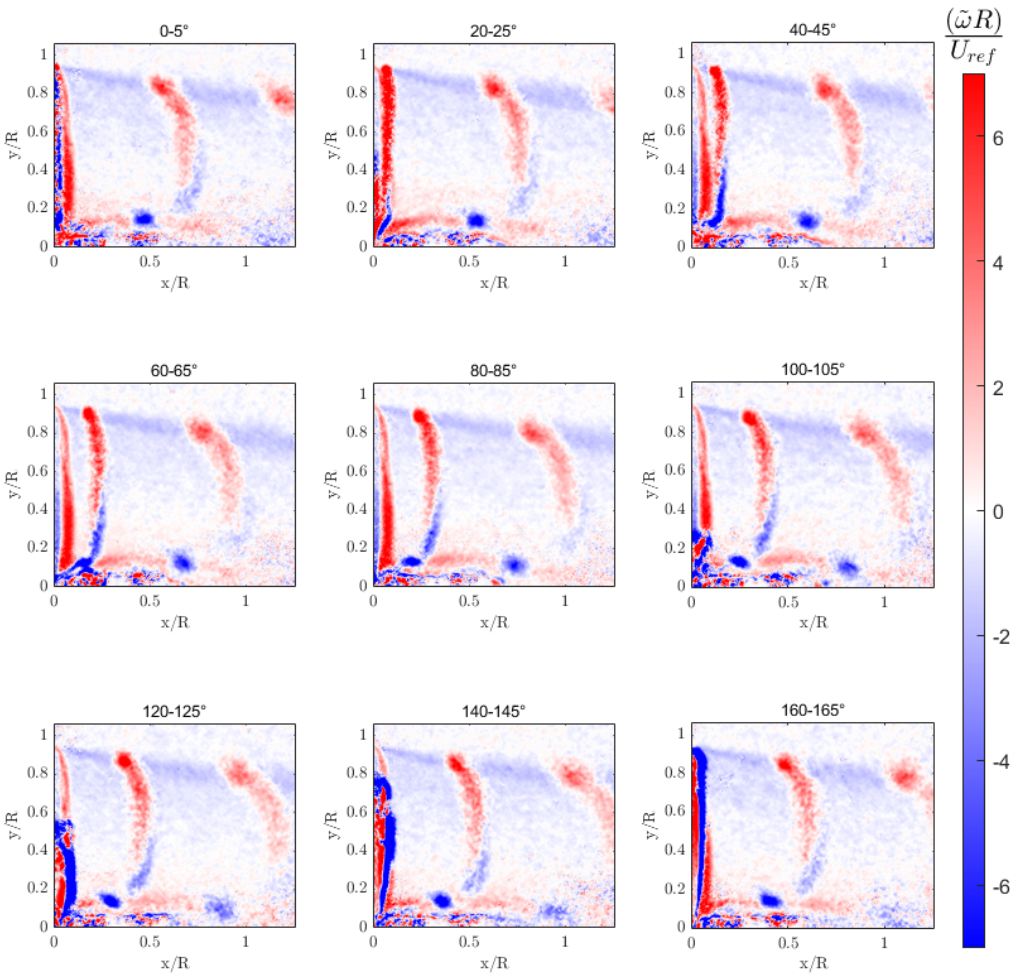

Figure 58: Periodic vorticity components of fluctuations $\tilde{\omega}$, SR4.

In Figure 58, the normalized periodic component of vorticity, $\tilde{\omega}$, obtained for the maximum shear-rate condition is shown. When comparing it with the same quantity in the uniform–flow case, some differences can be identified.

When transitioning from the uniform case to the maximum shear-rate condition, the vortex-tip structures travel downstream more rapidly and migrate outward in the radial direction. This result is consistent with the observations discussed in the previous sections. Furthermore, the vorticity in such structures appears to be less intense: even the shape of the vortices seems to be less defined.

Regarding the trailing-vortex-sheet region, in the uniform-flow case the structure tends to dissipate as it moves downstream (and, accordingly, the vorticity approaches zero); under the shear-rate condition, this effect still occurs, but the positive and negative components of the structure decay differently due to the flow asymmetry. Specifically, the negative component of the structure tends to dissipate already around 40–45°, whereas in the uniform case it remains clearly visible at the same blade azimuthal position.

The vortical structure induced by the motor geometry does not exhibit substantial differ-

ences in behavior. This is consistent with the nature of the generated flow: at the center of the propeller, the local velocity equals $U_{ref} = U_{\infty}$, and therefore no significant differences in behavior are expected relative to the uniform-flow case.

Performance evaluation

Effect of the shear flow

In order to study the effect of shear flow on the propeller, the position of the propeller was changed from the first to the second experimental setup.

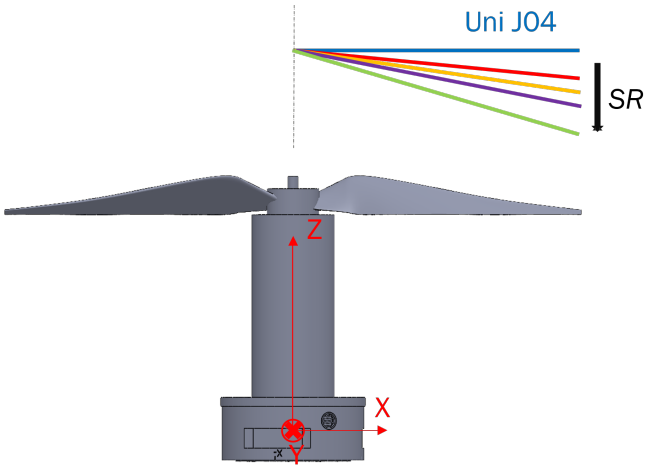

Figure 59: Shear flow - propeller interaction.

The propeller is positioned in such a way as to ensure that the flow meets the centre of the blade under uniform conditions, while at the tip of the blade it will impact the flow with the highest streamwise U velocity. The reference system used for the calculation of forces $(X - Y - Z)$ is shown in Figure 59 and is different from the one used for the study of propeller aerodynamics $(x - y - z)$: in this type of configuration, the thrust will have direction $Z+$, while the aerodynamic torque resistant to rotation by blade conformation will be directed in $Z-$.

The first objective was to acquire the forces on the propeller as the rotation speed increases, with the Windshaper off, in order to get an idea of the correct functioning of the setup.

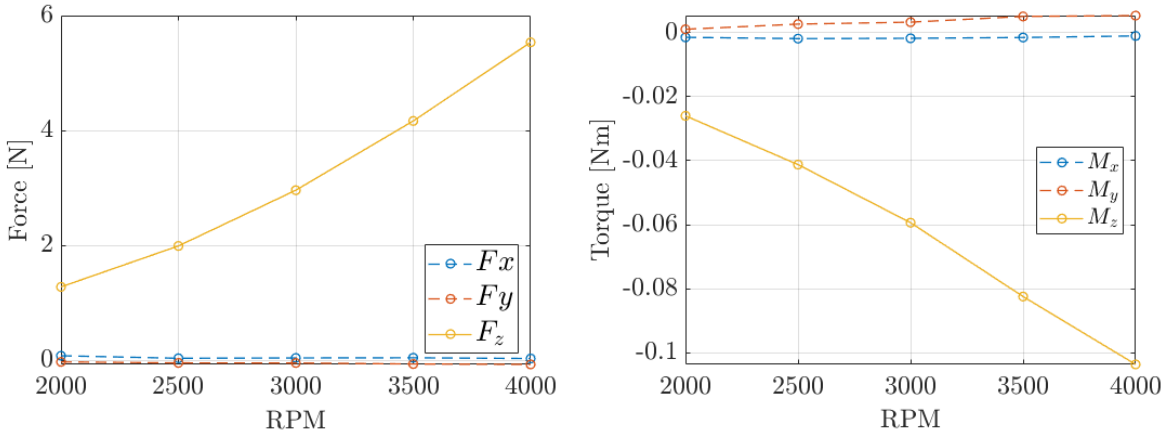

Figure 60: First test of loading cell: increasing RPM, $U_\infty = 0$.

Subsequently, a test was carried out under uniform flow conditions as J increased.

The results for force and torque are consistent with reality: as J increases, both thrust and torque decrease in absolute value. This can be seen from Figure 60, with the trends of C_t, C_q and η. The data were collected with J variable from 0 to 0.8, with the propeller rotating at a speed $\omega_{prop} = 2000RPM$ and a reference Reynolds equal to

$$Re = \frac{\rho U_{75\%R} c_{75\%R}}{\mu} \simeq 54000$$

With U and c evaluated 75% of the propeller radius.

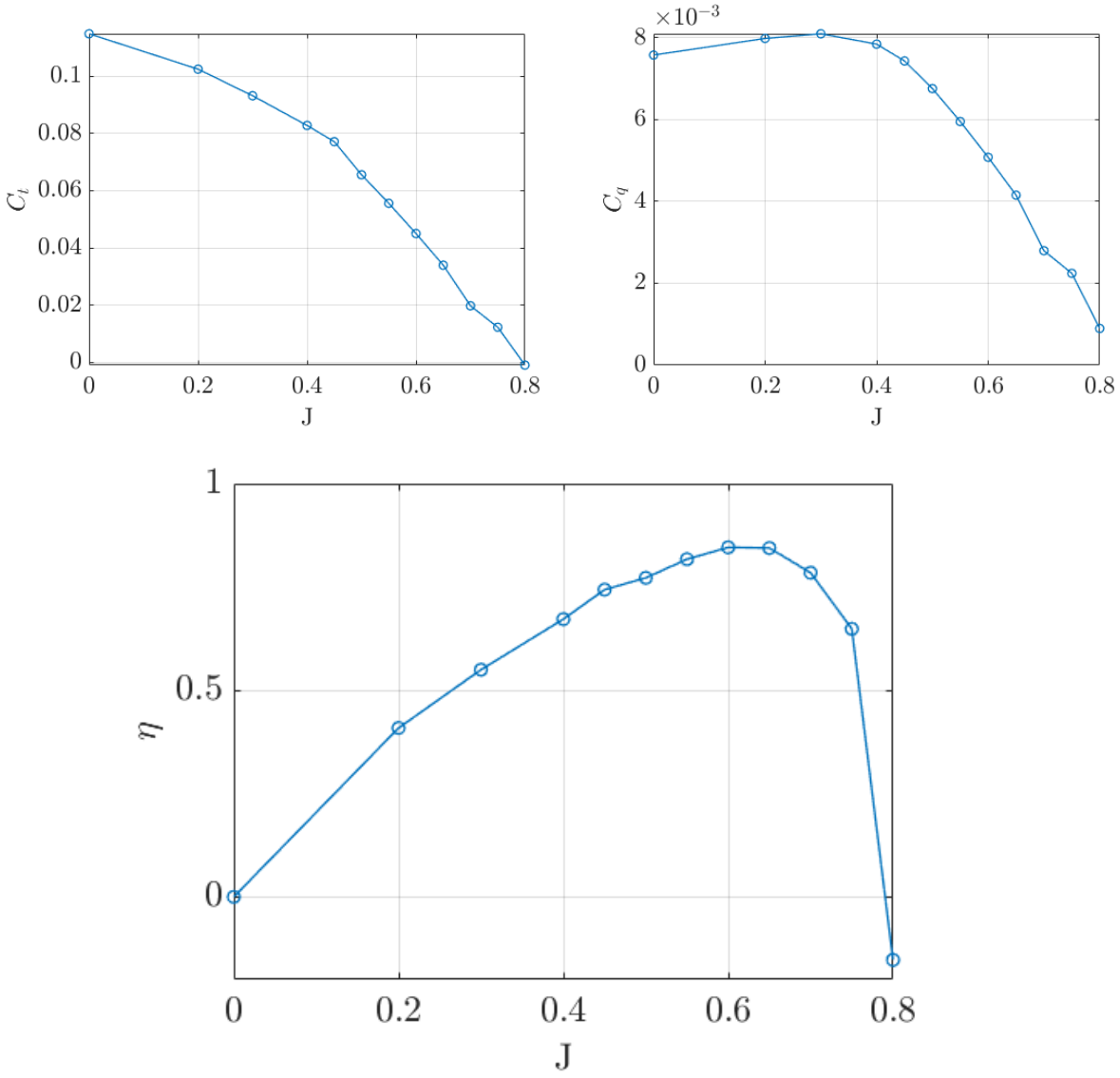

Figure 61: Thrust, torque and efficiency, uniform flow, 2000 RPM.

In Figure 61 then shows the trends of the thrust coefficient C_t and torque coefficient C_q, defined as:

$$C_t = \frac{F_Z}{\rho \left(\frac{N}{60}\right)^2 D^4}$$

$$C_q = \left| \frac{M_Z}{\rho \left(\frac{N}{60}\right)^2 D^5} \right|$$

While efficiency η:

$$\eta = \frac{C_t}{2\pi C_q}$$

The J of maximum efficiency settles around 0.6.

Relevant data were subsequently obtained by characterizing the forces under shear-flow conditions.

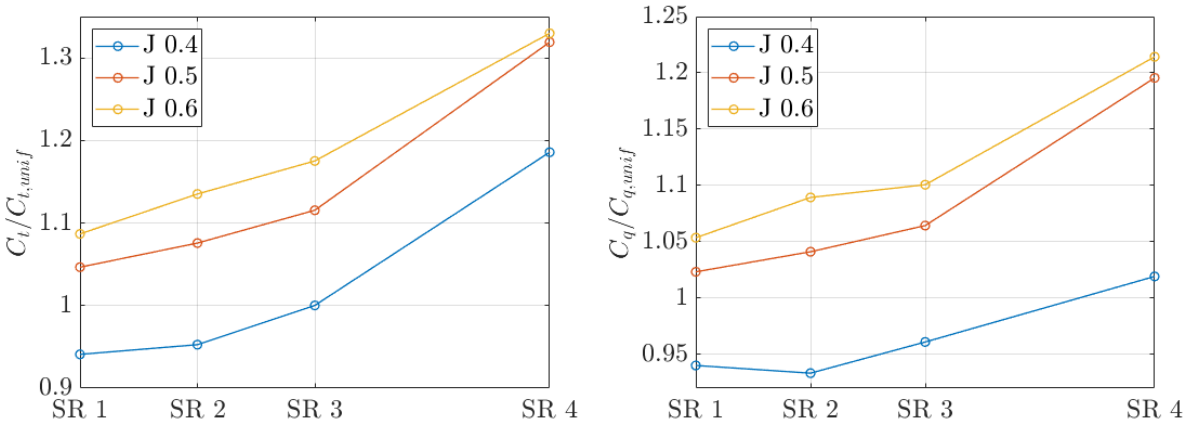

Figure 62: Thrust, torque with increasing Shear Rate SR.

Figure 62 shows the results for different J conditions: in the labels it is possible to distinguish the SR cases, while the ordinates show the thrust and torque coefficients, normalised to the respective coefficients in the case of uniform flow. In this visualisation, attention is drawn to the effect of shear flow, in particular how in most cases it increases the thrust coefficient; in particular, as J increases, this effect becomes more relevant, perhaps due to the presence of lower thrust and resistant torque levels. For $J = 0.4$, the first two shear flow cases instead show a reduction in the coefficients: these different types of behaviour could be due to the fact that along the blade the velocity profile changes and therefore the aerodynamic behaviour along the radius also changes locally. In general, however, the prevailing effect seems to be an increase in thrust and torque as the shear rate increases, as can be seen from the data for the fourth shear case.

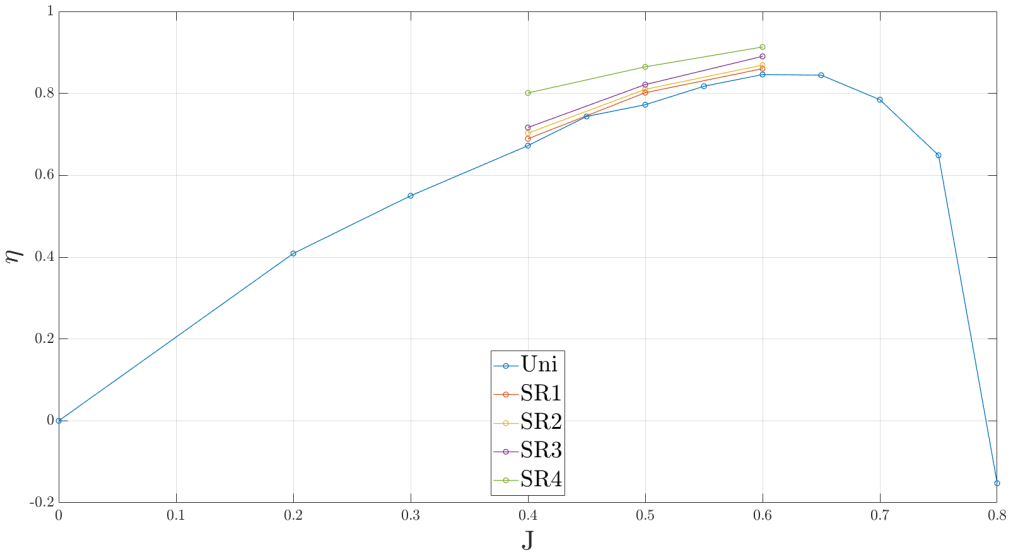

Figure 63: Efficiency map, with J and SR.

It is therefore interesting to evaluate the behaviour of the efficiency in the various cases, shown in Figure 63.

In general, the propeller seems to benefit from the presence of shear rate: propulsive efficiency increases compared to the uniform case, reaching a maximum in the SR 4 case with efficiencies greater than 0.8. The variation between $J = 0.4$ and $J = 0.6$ decreases as the shear rate increases, thus tending to flatten the results around $J = 0.6$, while in $J = 0.4$ the effect is very marked. Obviously, this only applies to the cases of J studied.

In addition to the effects on thrust and resisting torque, it is interesting to check whether the presence of shear flow also has consequences on forces and torques in directions other than Z: in particular, the presence of an additional torque M_y compared to the case of uniform flow is evident.

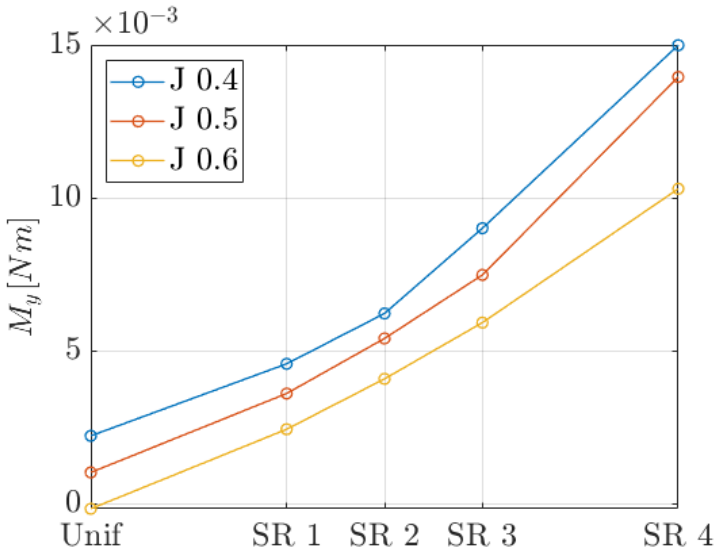

Figure 64: Effect of shear flow on M_y.

This additional torque, represented in Figure 64, is closely linked to the intensity of the shear rate; of rather modest value, it shows a decreasing trend as J increases.

Finally, as a further verification of the reliability of the data, repeatability tests were carried out. These tests were performed on different days, acquiring data in the case of uniform flow, as J increases.

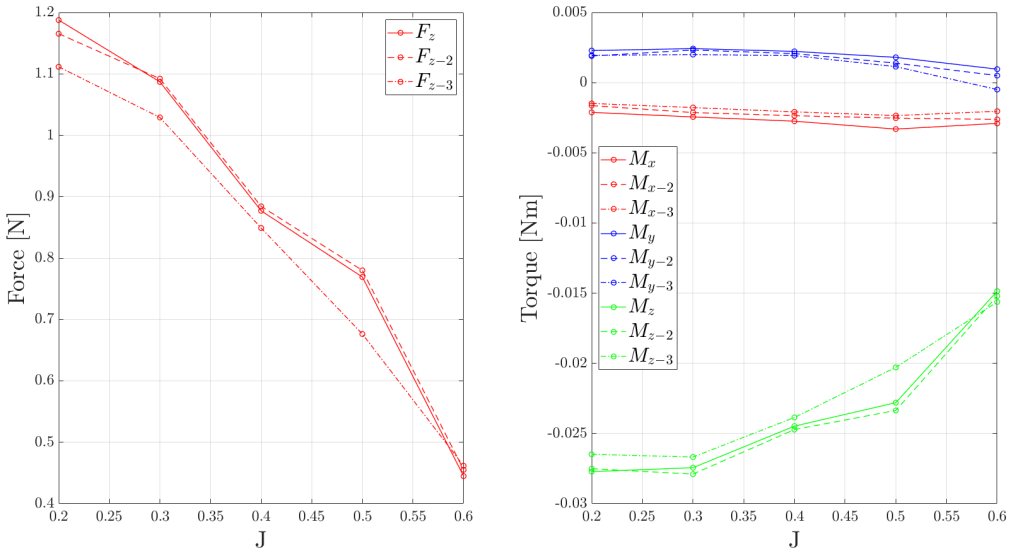

Figure 65: Repeteability test at uniform flow.

The maximum difference between two proofs turns out to be in the uniform case $J = 0.5$, between the second and third acquisitions, for a difference of approximately $13,8\%$.

Part V.
Conclusions

The work carried out has enabled an in-depth analysis of the interaction between a small propeller and a flow, both in the case of uniform flow and in the case of variable shear flow, through an experimental campaign conducted at the Modesto Panetti laboratory of the Polytechnic University of Turin. The flow was generated using a Windshaper facility, whose correct functioning was verified using a 5-hole probe. The forces acting on the propeller were measured using a load cell mounted on the support, while the propeller wake was characterised using PIV technology. The main objective was to assess how the presence of a velocity gradient affects the wake structure, turbulent fluctuations and propulsive performance, in order to improve understanding of the behaviour of drones in realistic operational scenarios, such as urban environments or those subject to strong atmospheric gradients.

Results: wake characterization

PIV analysis allowed to characterise a portion of the wake, obtaining over two thousand velocity fields over time, from which both time-averaged quantities and phase maps were derived. The results show that the introduction of shear flow significantly modifies the structure of the wake, in particular:

- Reduction in vorticity in tip vortices as the shear rate increases: the difference in speed between the back and front of the blade is reduced in the tip region, decreasing vorticity generation.
- Radial outward translation of vortices, consistent with the increase in local velocity imposed by the shear profile. This effect can be observed both in the average analyses and, more clearly, in the study of the position of the vortex centres.
- Increase in the convective velocity of the vortices, confirmed by the greater distance between successive vortices and their presence further downstream compared to the uniform case.
- Relatively stable behaviour of the trailing vortex sheet, whose intensity varies less with shear than the end vortices, consistent with its origin being mainly linked to the geometry of the problem.
- The behaviour of vortex structures was also analysed by studying turbulent kinetic energy κ: shear tends to dampen fluctuating components in the tip vortex zone, while the trailing vortex sheet region maintains more stable levels of turbulent energy.
- Through Reynolds decomposition and triple decomposition, a substantial part of the fluctuations, periodic and directly linked to rotation, was separated.

Results: interaction of shear rate with propulsion

The characterisation of the forces highlighted how shear flow has a significant influence on the performance of the propulsion system:

- In general, thrust and torque tend to increase as the shear rate increases, with a more pronounced effect at higher advance ratios.
- Propulsive efficiency η increases systematically with shear, reaching values greater than 0.8 in the SR4 case. The curves also tend to flatten out as they approach the maximum efficiency value, $J = 0.6$.
- A further effect is the emergence of a lateral moment M_y that is absent in uniform flow conditions. Its intensity increases with the shear rate and decreases as J increases: this is particularly relevant in real-world applications.

This behaviour is consistent with what has been observed in the literature, as thrust generation varies along the propeller phase. One explanation for the increase in thrust can be traced back to an increase in the local velocity component incident on part of the disc, which can cause an increase in the effective angle of attack and therefore in the lift generated.

Limitations of the study and critical issues

Repeatability tests show adequate consistency of results, with maximum deviations of around 14%, which is acceptable considering the complexity of the measurements and the unstable nature of the flow.

However, certain limitations must be taken into account:

- Asymmetry of the wake and two-dimensionality of the technique: the PIV technique used is 2D2C, therefore it does not allow direct observation of the out-of-plane velocity component, which is essential for the complete reconstruction of vortices;
- RPM fluctuation: RPM fluctuation (± 80) introduces unavoidable variability in instantaneous measurements;
- Repeatability of force tests: a small percentage of tests were discarded because they were highly inaccurate.

Future developments

In conclusion, the work has highlighted how a small propulsion system interacts with a shear flow, providing a solid basis for future studies and representing a useful contribution to the design and control of vertical take-off aircraft.

The work opens up several future developments, including:

- Extending the analysis by studying the other half of the wake, either through stereoscopic or tomographic PIV, to reconstruct the three-dimensional component of the wake as well;
- The study of blades with different geometries, to separate the rotational fluctuation component and then compare the turbulence obtained from the triple decomposition;
- Tests in non-stationary flows or with gusts;
- Integration with advanced CFD simulations to expand the range of conditions that can be explored and validate the numerical results obtained.

References

[1] Golubnichiy Artem Aleksandrovich and Nedelina Darya Olegovna. Review and analysis of the modelling of the atmospheric air pollution for urban air basins. 7:120, 2015.

[2] WeatherDecTech. https://medium.com/@weatherdectech/how-do-sea-breezes-work-a2717d377e34.

[3] Alberto Susini. A technocritical review of drones crash risk probabilistic consequences and its societal acceptance. *Lnis*, 7:27–38, 2015.

[4] Mojtaba Hedayatpour, Mehran Mehrandezh, and Farrokh Janabi-Sharifi. Propeller performance in presence of freestream. 2018.

[5] Chuansheng Zhang, Shengguang Xie, and Tianhao Pin. Aerodynamic analysis of small propeller in wind field using cfd. In *2015 4th International Conference on Sustainable Energy and Environmental Engineering*, pages 850–858. Atlantis Press, 2016.

[6] Motonao Murakami, Hiroyuki Abe, Hikaru Aono, and Hitoshi Ishikawa. Effects of gusty flow on aerodynamic performance of multirotor drone propellers in hovering flight. *Journal of Fluid Science and Technology*, 17(4):JFST0013–JFST0013, 2022.

[7] Linpeng Wang, Yuting Dai, and Chao Yang. Gust response analysis for helicopter rotors in the hover and forward flights. *Shock and Vibration*, 2017(1):8986217, 2017.

[8] MA Kotb and JA Schetz. Measurements of three-dimensional turbulent flow behind a propeller in a shear flow. *AIAA journal*, 24(4):570–577, 1986.

[9] Windshape. https://windshape.com/products/.

[10] Flavio Noca, Guillaume Catry, Nicolas Bosson, Luca Bardazzi, Sergio Márquez, and Albéric Gros. Wind and weather facility for testing free-flying drones. In *AIAA Aviation 2019 Forum*, page 2861, 2019.

[11] G.V. Saikiran and N. Seshaiah. Design and analysis of a five hole pressure probe using different materials. *Journal of Emerging Technologies and Innovative Research (JETIR)*, 6(6):749–751, 2019. ISSN-2349-5162.

[12] Zaber. https://www.zaber.com/products/linear-stages.

[13] ATI Industrial Automation. https://www.ati-ia.com/products/ft/ft_models.aspx?id=gamma.

[14] Scanivalve Corporation. *DSA3200 User Manual, Version 1.18*, 2021. Available online: https://scanivalve.com/media/27999/dsa3200v118.pdf (accessed May 2, 2025).

[15] Damiano Casalino, Edoardo Grande, Gianluca Romani, Daniele Ragni, and Francesco Avallone. Definition of a benchmark for low reynolds number propeller aeroacoustics. *Aerospace Science and Technology*, 113:106707, 2021.